Crustal growth identified by high-$\delta^{18}O$ zircon and olivine: A perspective from ultramafic arc cumulates in southern Tibet

Jun Wang[1,2], Qiang Wang[1*,2,3], Peng Sun[1], Wei Dan[1,2], Andrew C. Kerr[4], Zhi-Ping Zhang[5], Le Zhang[1,2], Gangjian Wei[1,2], Han Dong[5], Wan-Long Hu[1,2], Zong-Yong Yang[1,6], Xiu-Zheng Zhang[1,2], Yue Qi[1,2]

[1]State Key Laboratory of Isotope Geochemistry, Guangzhou Institute of Geochemistry, Chinese Academy of Sciences, Guangzhou, 510640, China

[2]CAS Center for Excellence in Deep Earth Science, Guangzhou, 510640, China

[3]College of Earth and Planetary Sciences, University of Chinese Academy of Sciences, Beijing 100049, China

[4]School of Earth and Environmental Sciences, Cardiff University, Cardiff, CF10 3AT, UK

[5]The Third Institute of Geology and Minerals Exploration, Gansu Provincial Bureau of Geology and Minerals Exploration and Development, Lanzhou 730050, China

[6]State Key Laboratory of Ore Deposit Geochemistry, Institute of Geochemistry, Chinese Academy of Sciences, Guiyang, 550081, China

CORRESPONDING AUTHOR:

*Qiang Wang, State Key Laboratory of Isotope Geochemistry, Guangzhou Institute of Geochemistry, Chinese Academy of Sciences, Wushan Street, Guangzhou, 510640; Tel: +86-20-85290277, Fax: 86-20-85290130; E-mail: wqiang@gig.ac.cn

ABSTRACT

In recent studies of crustal growth using global zircon Hf–O isotopic datasets, high-$\delta^{18}O$ zircons are typically attributed to intra-crustal reworking during which very little juvenile mantle-derived magmas were added to the crust. Although arc magmas may originate from a high-$\delta^{18}O$ mantle wedge, it has been difficult to decipher the contribution of high-$\delta^{18}O$ mantle to zircon-saturated felsic magma due to superimposed intra-crustal processes. We address this issue by combining the data from high-$\delta^{18}O$ zircon-bearing ultramafic cumulates and coeval lavas from a Cretaceous magmatic arc in southern Tibet. The cumulates mainly consist of different proportions of cumulus olivine and intercumulus amphibole. Amphibole analyses show a transition from increasing to decreasing Zr with increasing SiO_2 (50–74 wt.%) contents in the intercumulus melts, indicating zircon saturation in late-stage interstitial melts. The εNd(t) values (2.4 ± 1.4) of the apatite grains crystallised before and after zircon remain almost constant. Interstitial zircons have $\delta^{18}O$ (6.1–7.2‰) values similar to the earliest crystallised olivine ($\delta^{18}O$ = 6.3–7.1‰) in the cumulates. The coeval lavas may represent the intercumulus melts extracted from amphibole-rich cumulates at different depths. Both the lavas and cumulates were ultimately derived from high-$\delta^{18}O$ arc mantle modified by small amounts (<12%) of subducted sediments, and crystallised zircon during intra-crustal magma evolution without involving crustal contamination or melting. These high-$\delta^{18}O$ zircons therefore are not products of crustal reworking, but record crustal growth during their crystallisation (110 ± 2 Ma). Our study shows that the combination of zircon and olivine oxygen isotopes for ultramafic to felsic rocks is more effective than zircon data alone in evaluating the role of crustal growth vs. reworking in an arc system. The implication is that global zircon-based crustal evolution models that attribute all

high-$\delta^{18}O$ zircons to crustal reworking may conceal recent crustal growth.

KEYWORDS: crustal growth; zircon; olivine; oxygen isotope; Tibet

INTRODUCTION

The mechanisms and rates governing the formation of Earth's continental crust are a fundamental topic in Earth sciences (e.g. Armstrong, 1981; Arndt, 2013; Hawkesworth et al., 2010; Rudnick, 1995). Answering this question requires a knowledge of the balance between crustal growth and reworking throughout Earth's history (e.g., Dhuime et al., 2012; Kemp et al., 2006; Roberts and Spencer, 2015). Crustal growth involves the addition of mantle-derived magmas to the crust, whereas crustal reworking is the remobilization of pre-existing crust by melting and/or erosion and sedimentation (Hawkesworth et al., 2010). Individual magmatic events may involve crustal growth, reworking, or a combination of the two processes. Due to crustal reworking, the original ages (e.g., before 2.5 Ga) of ancient crustal formation have only rarely been preserved, and as a result present-day surface ages are expected to be biased to younger ages.

Our understanding of the evolution of the continental crust has been enhanced by U–Pb, Hf and O isotopic analyses in zircon. Hafnium isotopes in zircon are used to date the time since the crustal source(s) of the zircon-hosting magma were extracted from a mantle reservoir, commonly referred to as the model or crustal residence age (DePaolo, 1981; McCulloch and Wasserburg, 1978). However, if zircon crystallised from a magma with mixed source rocks, the model age is a meaningless hybrid age that does not represent true periods of crustal growth

(Arndt and Goldstein, 1987). The most common mixed sources are sedimentary rocks that have experienced low-temperature water-rock reaction and typically have elevated $\delta^{18}O$ (ca. 7–35‰; Bindeman, 2008). Thus, O isotopes in zircon are widely used to distinguish model ages of crust formation from hybrid ages (e.g., Hawkesworth and Kemp, 2006; Iizuka et al., 2013; Dhuime et al., 2012). These studies rely on two assumptions: (1) zircons crystallised from mantle-derived magmas have a narrow range of $\delta^{18}O$ (5.3 ± 0.6‰, 2SD; Valley et al. 1998) and record true periods of crustal growth; (2) high-$\delta^{18}O$ (>5.9‰) zircons record periods dominated by the reworking of supracrustal rocks.

These assumptions have recently been questioned (Cornet et al., 2022; Couzinié et al., 2016; Dan et al., 2015; Payne et al., 2016; Roberts and Spencer, 2015). Mass balance calculations indicate that at least 80% of the continental crust was generated at subduction zones (Rudnick, 1995). However, the mantle source of arc magmas can be enriched in ^{18}O by reaction with high-$\delta^{18}O$ fluids or melts derived from subducting slabs (including the hydrated oceanic crust and sediments) over millions of years (Auer et al., 2009; Bindeman et al., 2005; Dorendorf et al., 2000; Johnson et al., 2009; Martin et al., 2011). This means that the high-$\delta^{18}O$ signature of zircons may result from source contamination of the mantle wedge by slab-derived material, crustal contamination of mantle-derived magmas, or simple remelting of supracrustal rocks. High-$\delta^{18}O$ zircons formed by the first mechanism could be incorrectly attributed to crustal reworking based on the interpretation of Hf–O isotopes in detrital zircons on a global scale (e.g., Cornet et al., 2022; Couzinié et al., 2016). Elucidating the mechanism of high-$\delta^{18}O$ zircon formation, is therefore essential for identifying whether its parent magma contributed to crustal growth during its crystallisation.

Felsic magmatic rocks (e.g., granitoids), as the main host rock for zircon, can be produced during crustal reworking (i.e., remelting of older crustal lithologies) or growth (i.e., differentiation of mantle-derived magmas; Moyen et al., 2017). Mantle source compositions can be difficult to identify in crustal magmatic systems that have undergone magma differentiation and so it can be difficult to determine if mantle-derived magmas play a key role in the formation of high-$\delta^{18}O$ zircons.

In this paper we present detailed geochronological, mineralogical and geochemical data from high-$\delta^{18}O$ zircon-bearing ultramafic cumulates from a Cretaceous magmatic arc in southern Tibet that have enabled us to see through crustal processes. We combine zircon, olivine and apatite multi-isotope data from cumulates, with data from coeval lavas. These data have enabled us to decipher the contribution of crustal contamination to high-$\delta^{18}O$ zircon saturation, evaluate the role of crustal growth vs. reworking during this Cretaceous magmatic episode, and tentatively explore the potential biases introduced by zircon Hf–O isotopes in global zircon-based crustal evolution models.

GEOLOGICAL SETTING AND PETROGRAPHY

The Lhasa Terrane in the southern Tibetan Plateau is separated from the Qiantang Terrane by the Bangong–Nujiang suture to the north and from the Himalaya Terrane by the Indus–Yarlung Zangbo suture to the south. The Lhasa terrane can be can be divided into southern, central, and northern subterranes by the Luobadui–Milashan fault and Shiquan River–Nam Tso mélange, respectively (Fig. 1a). Sedimentary cover in the northern Lhasa subterrane consists of Triassic-Cretaceous strata and exposures are dominated by extensive

Lower Cretaceous volcano–sedimentary sequences of the Duoni and Qushenla formations, and coeval plutons (Fig. 1b). Zircon Hf isotopic mapping (Hou et al., 2015; Lu et al., 2017; Zhu et al., 2011) has revealed that the western segment (west of E88°) of the northern Lhasa subterrane is a juvenile Phanerozoic crustal block (Fig. 1a) with high εHf values (up to +15) and young Hf model ages (as young as 200 Ma). The Yanhu area is located at the heart of this juvenile crustal block and magmatism around Yanhu occurred from 131 to 110 Ma. This magmatism has been attributed to rollback and breakoff of the south dipping Bangong–Nujiang Tethyan slab (Hao et al., 2016; Li et al., 2018) or northward subduction of the Indus–Yarlung Zangbo Tethyan slab at a low angle (Zeng et al., 2020). Multidisciplinary studies of magmatic rocks, paleomagnetism, and sedimentology show that the western segment of the Bangong–Nujiang Tethyan Ocean closed later (<110 Ma) than its eastern–middle segments (Hu et al., 2022 and references therein). Therefore, it is likely that the Early Cretaceous magmatism around Yanhu was related to oceanic subduction, although questions remain as to which of two opposite-dipping slabs played a dominant role.

The Yanhu ultramafic pluton (~0.05 km^2; Fig. 1c) intrudes Upper Jurassic strata comprising metamorphosed volcanic rocks intercalated with sandstones (Supplementary Fig. S1). It has an orthocumulate texture, consisting of 35–60 vol% olivine, 25–55 vol% amphibole, 5–10 vol% orthopyroxene, <5 vol% clinopyroxene (Table S1), and trace amounts of phlogopite, spinel, apatite, and zircon (Fig. 2). Nine samples (Latitude: 32°27′03″N; Longitude: 83°18′59″E) were collected that contained variable proportions of olivine and amphibole. Four samples are olivine hornblendites containing more amphibole than olivine; the other samples are hornblende peridotite (Table S1). The main cumulus phase is olivine (Fig. 2a–b), which contains spinel

inclusions and is partially altered to serpentine. The intercumulus space is filled with amphibole and orthopyroxene (Fig. 2a–b). Numerous spatially separated, but optically continuous amphibole grains form large oikocrysts that poikilitically enclose smaller grains of olivine and clinopyroxene (Fig. 2a–c). Orthopyroxene also contains olivine inclusions (Fig. 2d), but clinopyroxene inclusions are not observed in orthopyroxene. Olivine and clinopyroxene inclusions are characterized by rounded and irregular shapes or embayed rims (Fig. 2a–d). These disequilibrium textural characteristics indicate that the amphibole and orthopyroxene grew at the expense of olivine and clinopyroxene. Some amphibole crystals have wide, brown cores with narrow, green rims (Fig. 2a–b). Scarce green amphibole (<5 vol.%) can also be found as larger grains between olivine and brown amphibole (Fig. 2c). Two zircon grains are observed in interstitial phlogopite (Fig. 2e). Apatite can coexist with clinopyroxene and can occur both as early-crystallised inclusions within large amphibole oikocrysts (Fig. 2f), and as a late interstitial phase between the intercumulus orthopyroxene and amphibole (Fig. 2g), indicating a wide range of crystallisation temperatures.

ANALYTICAL METHODS

Zircon U–Pb, Hf and O isotopes

Zircons were separated using conventional heavy liquid and magnetic separation techniques (Li and Tan, 1998), and then were mounted in epoxy and polished. To characterize zircon internal structures and choose target sites for isotopic analyses, cathodoluminescence (CL) images were obtained using a Carl Zeiss Field Emission Scanning Electron Microscope + Gatan MonnCL4. U–Th–Pb isotopic analyses were conducted using a Cameca IMS-1280-HR Secondary Ion Mass

Spectrometer (SIMS). The analytical procedures were the same as those described by Li et al. (2009). The O_2^- primary ion beam with an intensity of ~10 nA was accelerated at –13 kV, and the ellipsoidal spot was about 20 × 30 μm in size. U–Th–Pb ratios were determined relative to the ~337 Ma standard zircon Plešovice (Sláma et al., 2008). A second zircon standard (Qinghu; Li et al., 2013) was alternately analyzed as an unknown together with other unknown zircons. Nine analyses of the Qinghu zircon yielded a concordia age of 159.2 ± 1.6 Ma, which is within error of the recommended value of 159.5 ± 0.2 Ma (Li et al., 2013). The weighted-mean U–Pb ages and concordia plots were processed using Isoplot v. 3.0 (Ludwig, 2003).

Zircon oxygen isotopes were measured using the same Cameca IMS-1280-HR SIMS. The detailed analytical procedures were similar to those described by Li et al. (2010). The Cs^+ primary ion beam was accelerated at 10 kV, with an intensity of ca. 2 nA, and rastered over a 10 × 10 μm area. The spot size was about 20 μm in diameter. The measured oxygen isotopes were corrected for instrumental mass fractionation using the Penglai zircon standard ($\delta^{18}O_{VSMOW}$ = 5.3‰; Li et al., 2010). The internal precision of all single analyses were better than 0.28‰ (2σ; Table S3) for the $^{18}O/^{16}O$ ratio. The external precision, measured by the reproducibility of repeated analyses of the Penglai standard, is 0.22‰ (1σ; n = 15). Eight measurements of the Qinghu zircon standard yielded a weighted-mean $\delta^{18}O$ of 5.3 ± 0.3‰ (2σ), within error of the reported value of 5.4 ± 0.2‰ (Li et al., 2013).

Zircon Hf isotopic analyses were undertaken using a Neptune Plus MC–ICP–MS equipped with a RESOlution M-50 193 nm laser ablation system (Resonetics), with a beam diameter of 45 μm. Analytical procedures have been given by Wu et al. (2006). Analyses of the Plešovice zircon standard yielded a weighted mean of $^{176}Hf/^{177}Hf$ = 0.282479 ± 0.000013 (1σ; n = 15), consistent

with the certified value of 0.282482 ± 0.000013 (2SD; Sláma et al., 2008). Zircon Hf model ages (T_{DM}) were calculated using the reference line for the Hf isotope evolution of the depleted mantle (DM; Griffin et al., 2000) and assuming $^{176}Lu/^{177}Hf$ = 0.015 for the source of magmas from which the zircon crystallised. Zircon U–Pb and Hf–O isotopic data are presented in Tables S2 and S3, respectively.

Whole-rock geochemistry

The samples for whole-rock chemical analyses were crushed to coarse chips in a jaw crusher having corundum jaws and fresh pieces were hand-picked. The rock chips were rinsed twice with deionized water, dried, and then powdered to ~200 mesh size in an agate mortar and pestle that was free from metal contamination. Samples were prepared as glass discs using a Rigaku desktop fusion machine, formed by mixing 0.50 g of rock powder with 4.0 g of lithium tetraborate for 15 min at 1100°C in 95%Pt–5%Au crucibles. Major-element oxides were analyzed on fused glass beads using a Rigaku RIX 2000 X-ray fluorescence spectrometer following the procedures of Li et al. (2006). Interference-corrected spectra were converted to concentrations using a calibration curve consisting of 36 standard samples. Reproducibility, as gauged from the repeated analyses of two USGS reference materials (BHVO-2 and BCR-2), is better than 4 % (RSD, relative standard deviation; Table S1). Trace elements, including rare earth elements (REE), were analyzed by inductively coupled plasma–mass spectrometry (ICP–MS), using a Perkin-Elmer ELAN 6000 instrument following the procedures described by Li et al. (2006). About 40 mg of each powdered sample was dissolved in a high-pressure Teflon bomb for 2 days at 190°C using $HF+HNO_3+HClO_4$ (1:1:0.2) mixtures. Analytical precision, measured by the reproducibility of

repeated analyses of two USGS reference materials, is better than 5% (RSD; Table S1) for most elements. The remaining elements (Pb, Cs, Sc, and Ge) have the RSD values of 5-10%.

Neodymium isotopic compositions were determined on a Neptune Plus multicollector (MC) ICP–MS (Thermo Scientific), using the analytical procedures described by Li et al. (2006). Neodymium fractions were separated by passing through cation columns followed by HDEHP columns. Measured $^{143}Nd/^{144}Nd$ ratios were normalized to $^{146}Nd/^{144}Nd = 0.7219$. Reference standard solutions (Shin Etsu JNdi-1) analyzed along with unknowns yielded $^{146}Nd/^{144}Nd$ values of 0.512121 ± 0.000011 (2SD, n=11). The basaltic standard BHVO-2 was used to monitor ion-exchange chromatographic purification processes, yielding $^{143}Nd/^{144}Nd$ values of 0.512989 ± 0.000008, consistent within errors with the recommended values of 0.512983 ± 0.000010 (Weis et al., 2005). Whole-rock elemental and isotopic data of the samples and basaltic standard are listed in Table S1.

Mineral major and trace elements

In situ major element analyses of apatite and olivine with spinel inclusions in epoxy, and amphibole and pyroxene in thin section were obtained using a JEOL JXA-8100 electron probe microanalyser (EPMA). The operating conditions were a 15 kV accelerating voltage, a 20 nA beam current, and a beam size of 1–2 μm. The data reduction was carried out using ZAF correction (Huang et al., 2010). If the analyzed olivine contains spinel, the EPMA spots of olivine are close to spinel inclusions to obtain olivine-spinel Al-exchange crystallisation temperatures (Fig. 3a). Given the great uncertainty of the olivine Al content analyzed by EPMA, we only used the Al content of olivine near spinel inclusions measured by LA–ICP–MS to calculate equilibrium temperatures (Fig.

3a).

In situ mineral trace-element compositions were determined using an ELEMENT XR ICP–MS coupled with a RESOlution M-50 193 nm laser ablation system. The laser was set up as follows: beam size, 33 μm; repetition rate, 6 Hz; energy density, ~4 J cm^{-2}. A smoothing device (The Squid, Laurin Technic) was used to smooth the sample signal. More details on the experiment procedure and data reduction strategy are described in detail by Zhang et al. (2019). Trace element concentrations were calibrated using multiple reference materials (BCR-2G, BHVO-2G, and GSD-1G) as external standards, and Ca and Si as the internal standard elements for apatite and silicate minerals, respectively. Laser spots were coincident with EPMA spots where possible, so that Ca and Si contents obtained using the EPMA could be used for internal standardization. Contamination from inclusions and fractures was monitored using several elements (e.g., Pb and REE). A reference glass TB-1G was measured as unknown samples. Repeat analyses (n = 24; Table S12) of the TB-1G reference glass during this study indicated that precision and accuracy were better than 10% for the elements of interest. Mineral major- and trace-element compositions are reported in Tables S4–S10.

Olivine oxygen isotopes

Olivine grains from two samples were mounted in epoxy and polished. The backscattered electron (BSE) images indicate that one (WQ09-1) of the samples contains sufficiently large olivine grains with few serpentinized fractures (Fig. 3a), which can be used for *in situ* analyses. Olivine was first analyzed by EPMA for major elements, then by SIMS for oxygen isotopes, and finally by LA–ICP–MS for Al contents. Laser ablation and SIMS spots were analysed in the same

location as EPMA spots (Fig. 3a). *In situ* oxygen isotopes were determined using a Cameca IMS-1280-HR SIMS. The beam size was about 10-15 μm. The analytical procedures, instrument conditions, calibration and data reduction are the same as given in Yang et al. (2018). Five unknown and two standard (San Carlos and 06JY29) $\delta^{18}O$ measurements were run in bracketed mode. Measured $^{18}O/^{16}O$ was normalized using the Vienna Standard Mean Ocean Water composition (VSMOW, $^{18}O/^{16}O = 0.0020052$). The measured oxygen isotopic data were corrected for instrumental mass fractionation (IMF) using the San Carlos olivine standard. The experience from the Cameca IMS 1270, 1280 and 1290 labs worldwide indicates that matrix effects resulting from variable Fo (molar 100 × Mg/ [Mg + Fe]) in olivine on the measured oxygen isotope ratios is not significant, provided that the olivine is characterized by Fo values ranging from 60 to 100 (e.g., Bindeman et al., 2008; Isa et al., 2017; Tang et al., 2019). For example, Bindeman et al. (2008) observed a systematic difference of IMF for San Carlos (Fo = 90) and CI114 (Fo = 74) olivine of 0.12‰, which equates to 0.0075‰ of IMF per each Fo number. Accordingly, a difference of IMF for the Yanhu olivine (Fo = 79-82) is less than 0.1‰, which is negligible and within error of our measurements. To monitor the external uncertainties, a second olivine standard (06JY29; Fo = 91.2) was alternately analyzed as an unknown together with other unknown olivines. Measurements on 06JY29 olivine yielded a $\delta^{18}O$ value of 5.25 ± 0.21 ‰ (1σ, n = 11), which is within error of the recommended value of 5.30 ± 0.13 ‰ (Tang et al., 2019). Olivine oxygen isotopic data are presented in Table S4.

Apatite Nd isotopes

Apatite grains from olivine hornblendite (WQ09-1) were mounted in epoxy and polished.

The BSE images (Fig. 3b) were used to select large grains lacking micro-pores and mineral inclusions for chemical analyses. *In situ* apatite Nd isotope analysis was carried out on a Neptune Plus MC–ICP–MS, coupled with a RESOlution M-50 193 nm laser ablation system. Apatite was first analyzed by EPMA for major elements, then by LA–ICP–MS for trace elements, and finally by LA–MC–ICP–MS for Nd isotopes. The laser spots were analysed in the same spots as the EPMA (Fig. 3b). The laser parameters were set as beam diameter of 112 μm, repetition rate of 7 Hz and energy density of ~4 J cm^{-2}. The interference of ^{144}Sm on ^{144}Nd was calculated with the signal of ^{147}Sm and the natural $^{144}Sm/^{147}Sm$ ratio of 0.20504 (Wasserburg et al., 1981). The mass bias factor of Sm was calculated from the measured ratio of $^{147}Sm/^{149}Sm$ and its accepted ratio of 1.08507 (Wasserburg et al., 1981). The mass bias of $^{143}Nd/^{144}Nd$ was normalized to $^{146}Nd/^{144}Nd$ = 0.7219 with an exponential law. The detailed instrumental conditions and data reduction procedure have been reported in Zhang et al. (2021). Every five analyses of our apatite were followed by one analysis of Durango and McClure apatite standards. The nine analyses of Durango and McClure apatite during this study yielded $^{143}Nd/^{144}Nd$ ratios of 0.512485 ± 0.000022 (2σ) and 0.512262 ± 0.000042 (2σ), which are, respectively, consistent within errors with the reported values of 0.512493 ± 0.000021 and 0.512282 ± 0.000011 (Yang et al., 2014). Apatite Nd isotopic data are given in Table S11.

RESULTS

Whole-rock elemental and Nd isotope, zircon U–Pb–Hf–O isotope, olivine O and apatite Nd isotope, and mineral major- and trace-element data for the Yanhu ultramafic cumulates are presented in the Supplementary Materials (Tables S1–11). All analyses were carried out at the

290 Guangzhou Institute of Geochemistry, Chinese Academy of Sciences in Guangzhou, China.

291

292 **Zircon U–Pb, O and Hf isotopic compositions**

293 Zircon U–Pb concordia diagrams and representative CL images for the Yanhu cumulates are
294 given in Fig. 4. Zircon CL images show no or broad-banded zoning in the core, and oscillatory
295 zoning in the rim (Fig. 4c–d), comparable to those reported for zircons from oceanic gabbros (e.g.,
296 Grimes et al., 2009). Thirteen of fifteen spot analyses from hornblende peridotite (D1131) and
297 eleven of thirteen spot analyses from olivine hornblendite (WQ09-1) yielded weighted-mean
298 $^{206}Pb/^{238}U$ ages of 110 ± 2 (2σ) Ma (Fig. 4 a–b), which are interpreted as the crystallisation ages of
299 the Yanhu cumulates. The remaining four analyses plot below or above the concordia curve,
300 probably due to radiogenic Pb loss or high common Pb (Table S2), respectively.

301 Zircon O and Hf isotope analyses were conducted on the same grains that were analyzed for
302 U–Pb dating. Zircon grains from hornblende peridotite (D1131) and olivine hornblendite
303 (WQ09-1) have indistinguishable $\delta^{18}O$ values of 6.1–6.9‰ and 6.1–7.2‰, respectively (Fig. 5a).
304 Therefore, zircon $\delta^{18}O$ values (6.7 ± 0.6‰ (2SD)) of the Yanhu cumulates are higher than normal
305 mantle zircon values of 5.3 ± 0.6‰ (2SD; Valley et al. 1998). Zircon εHf(t) values of hornblende
306 peridotite (D1131; εHf(t) = 9.9–13.3) and olivine hornblendite (WQ09-1; εHf(t) = 9.0–13.7) also
307 mostly overlap, with an average of 11.5 ± 2.2‰ (2SD) (Fig. 5a). Zircon Hf model ages vary from
308 291 to 596 Ma (Table S3).

309

310 **Whole-rock geochemistry**

311 The 110 ± 2 Ma Yanhu magmatic rocks include ultramafic cumulates from this study, and

312 non-cumulate basalts, andesites, rhyolites, and diorites reported by Sui et al. (2013) (Fig. 6). The
313 ultramafic cumulates have the highest MgO (27.6–32.8 wt.% on a volatile-free basis) and the
314 lowest SiO_2 (41.4–43.4 wt.%) contents of the Yanhu rocks (Fig. 6a). Within the ultramafic
315 cumulates, olivine hornblendites have higher CaO (5.3–6.5 wt%) contents than the hornblende
316 peridotites (CaO = 2.5–3.7 wt.%; Table S1). The REE patterns of all Yanhu rocks show an
317 enrichment in light REE (LREE) over middle REE (MREE) and heavy REE (HREE). The non-cumulate
318 rocks display a gradual decrease in MREE (e.g., Dy) contents from mafic to felsic rocks and a
319 MREE-depleted "trough-like" pattern characterizes the rhyolites (Fig. 6b). All of the Yanhu rocks
320 exhibit decreasing Dy/Yb ratios with increasing SiO_2 contents (Fig. 6c) and La/Sm ratios (Fig. 6d).
321 These differentiation trends are similar to those of some modern arc lavas, such as those from
322 the Aleutian, Java, and Lesser Antilles arc (Fig. 6c; Davidson et al., 2007). The Yanhu ultramafic
323 cumulates have homogeneous Nd isotopic compositions (εNd(t) = 2.3–3.5; Table S1).
324
325 **Mineral geochemistry**
326 Olivine in the ultramafic cumulates contains abundant spinel inclusions. No significant
327 Fe–Mg chemical zoning is observed within individual olivine and spinel inclusions (Fig. 3a).
328 Olivine has Fo values of 79–82 and CaO contents of 0.09–0.19 wt.% (Table S4). The Al content of
329 olivine close to spinel inclusions, measured by LA–ICP–MS (Fig. 3a), ranges from 63 to 101 μg/g
330 (Table S4). Spinel has a relatively narrow range of Cr# (molar Cr/[Cr + Al]) values of 0.60–0.67
331 (Table S5). Olivine has $\delta^{18}O$ values varying from 6.3‰ to 7.1‰, with an average of 6.7 ± 0.4‰
332 (2SD; n = 49), which are higher than typical mantle olivine values of 5.18 ± 0.28‰ (2SD; Mattey
333 et al. 1994; Fig. 5b).

334 The brown amphibole is pargasite with $(Na + K)^A > 0.5$ apfu (atoms per formula unit) and (Al
335 $+ Fe^{3+} + 2Ti)^C > 0.5$ apfu. Most of the green amphibole crystals are pargasites, but a small amount
336 of them are edenites with $(Al + Fe^{3+} + 2Ti)^C < 0.5$ apfu (Hawthorne et al., 2012; Table S6). The
337 brown amphibole contains higher TiO_2 (1.6–4.8 wt.%) and REE contents, but lower SiO_2
338 (41.1–44.8 wt.%) contents than green amphibole (TiO_2 = 0.2–1.1 wt.%, SiO_2 = 47.4–49.5 wt.%)
339 (Fig. 7a–b). Chondrite-normalized REE patterns of brown amphiboles are hump-shaped, with
340 LREE (e.g., La) and HREE (e.g., Yb) depletion relative to MREE (e.g., Sm) (Fig. 7b). Furthermore,
341 the brown amphiboles show a decrease in Dy/Yb with increasing La/Sm (Fig. 7c) and an increase
342 in Zr (81–233 μg/g) with increasing SiO_2 (Fig. 7d). Green amphibole is characterized by marked
343 LREE enrichment over MREE and HREE (Fig. 7b). Therefore, green amphibole has higher La/Sm
344 than brown amphibole, and its Dy/Yb is similar to that of high-La/Sm brown amphibole (Fig. 7c).
345 However, the Zr (57–156 μg/g) content of green amphibole is lower than the highest Zr content
346 (233 μg/g) in brown amphibole (Fig. 7d).

347 Clinopyroxene inclusions (Fig. 2c) in brown amphibole have Mg# (molar 100 × Mg/ [Mg + Fe])
348 values of 79.4–83.2 and CaO contents of 22.5–22.8 wt.%. The REE pattern of clinopyroxene is
349 subparallel to that of the host brown amphibole, but the clinopyroxene has lower REE contents
350 (Fig. 7b). Clinopyroxene inclusions have significantly lower Zr contents of 21–40 μg/g (Table S8)
351 than the host brown amphibole (Zr = 81–233 μg/g; Table S7). The intercumulus orthopyroxene
352 crystals have Mg# values of 80.6–82.1 and CaO contents of 0.9–1.3 wt.%, and they have very low
353 REE (e.g., La < 0.11 μg/g) and Zr (5.1–9.6) contents (Table S9).

354 Apatite is fluorapatite and hydroxyapatite and has CaO of 53.5–55.9 wt.% and P_2O_5 of
355 40.5–43.3 wt.%. It has variable F (1.3–2.4 wt.%) and Cl contents (0.4–2.1 wt.%) (Table S10), with

a positive correlation between ΣREE and Cl (Fig. 8a). Most of the apatite crystals show a homogeneous texture and lack micro-pores and mineral inclusions, and some crystals show a narrow, bright rim that has higher Cl than the dark core in BSE images (Fig. 3b). Thus, the variability of lightness on BSE images for apatite reflects a compositional difference, i.e., the bright domains are more enriched in REE and Cl than the dark domains, which are consistent with the detailed research by Krneta et al. (2016). Apatite shows marked LREE enrichment over HREE on chondrite-normalized REE diagrams (Supplementary Fig. S2). Its Dy/Yb ratio decreases with increasing La/Sm and Cl/F ratios (Fig. 8b–c). Apatite has $^{143}Nd/^{144}Nd$ ratios ranging from 0.512619 ± 0.000068 to 0.512753 ± 0.000063, corresponding to εNd(t) values of 1.2–3.6 (average = 2.4 ± 1.4; 2SD; n = 41). Apatite εNd(t) values are relatively invariant over a range of La/Sm (2.8 to 24.1), which is similar to its host rocks although their La/Sm ranges are different (Fig. 8d).

DISCUSSION

Post-magmatic alteration

Before using the mineral compositions to investigate their parent magmas, it is necessary to evaluate the influence of post-magmatic alteration. Interaction between olivine and hydrothermal fluids caused variable serpentinization along micro-fractures and rims of olivine as shown in Fig. 2a–c. Typical temperatures of serpentinization range from 100°C to 400°C (Wenner and Taylor, 1971). However, oxygen diffusion rates ($<10^{-25}$ m^2/s) at this temperature range are extremely slow (Chakraborty, 2010). Moreover, as the $\delta^{18}O$ values of olivine grains in the samples were determined by an *in situ* method, the analytical targets in the selected olivine grains were always away from micro-fractures (Fig. 3a). Thus, the $\delta^{18}O$ values of the Yanhu

olivine grains are not thought to have been affected by post-magmatic hydrothermal alteration.

Hoskin (2005) suggested that hydrothermally-altered or hydrothermal fluid-precipitated zircon usually occurs as rims on magmatic cores and less commonly as individual crystals, and the hydrothermal rims are internally textureless and non-luminescent in CL images whereas magmatic cores are oscillatory zoned. In contrast, the Yanhu zircon CL images show no or broad-banded zoning in the cores, and oscillatory zoning in the rims (Fig. 4c–d). The Th/U ratios of the studied zircons range from 1.0 to 21.3 (average = 4.2; Table S2) as commonly seen in magmatic zircons (Th/U > 0.5; Hoskin and Schaltegger, 2003). However, the zircons interpreted to be hydrothermal from the Boggy Plain Zoned Pluton aplite (Hoskin, 2005) and the Mole Granite (Pettke et al., 2005) have lower Th/U ratios (0.05 to 0.82) due to stronger mobility of U relative to Th in hydrothermal fluids. Hence, the studied zircons are magmatic in origin and their oxygen isotopes were not altered during post-magmatic hydrothermal activity.

Magmatic apatite may experience chemical and textural changes induced by hydrothermal fluids (Harlov, 2015). Compared with HREE and F, LREE and Cl in apatite preferentially partition into hydrothermal fluids. These fluids can then precipitate REE-bearing minerals, such as monazite (Broom-Fendley et al., 2016; Harlov, 2015; Krneta et al., 2016). Previous studies indicate that monazite is commonly found as inclusions in pore-bearing reacted areas that mostly occur along grain rims or cracks of hydrothermally-altered apatite, and these reacted areas are more depleted in REE and Cl, and so are darker than the unreacted areas in BSE images (Krneta et al., 2016; Zhang et al., 2020). However, most of the Yanhu apatite crystals are homogeneous and lack mineral inclusions, and some crystals have a bright rim in BSE images (Fig. 3b). They contrast markedly with partly altered apatites, which have bright cores and dark rims

that represent unreacted and preferentially reacted areas, respectively (e.g., Krneta et al., 2016; Zhang et al., 2020). In addition, the Yanhu apatite has a Dy/Yb versus La/Sm trend similar to coexisting amphibole, that is, its Dy/Yb ratio first decreases rapidly and then remains almost constant with increasing La/Sm (Fig. 7c and 8c). Thus, apatite and amphibole simultaneously record compositional changes in the intercumulus melts. Apatite occurs either as inclusions within amphibole or as a late interstitial phase between amphibole and orthopyroxene (Fig. 2f–g), also implying co-crystallisation with amphibole. The above chemical and textural evidence suggest that the variation in REE fractionation in apatite was not caused by hydrothermal activity.

The green amphiboles may form during subsolidus hydrothermal alteration given that some of them occur as replacive rims of the brown amphiboles. If green amphibole formed through reaction of brown amphibole with hydrothermal fluids almost devoid of fluid-immobile elements (e.g., Th), it should not contain a higher abundance of Th than its precursor of brown amphibole. However, the Yanhu green amphiboles indeed have a higher Th (1.23-2.08 μg/g) content than brown amphiboles (0.06-0.30 μg/g) (Table S7), which supports the magmatic nature of green amphiboles. Thorium will gradually concentrate in the residual melts during magma evolution as it is highly incompatible in olivine, pyroxene, and amphibole (Tiepolo et al., 2007). This is the reason for the difference in Th contents between the green and brown amphiboles. Moreover, green amphibole occurs not only as replacive rims of brown amphibole, but also as large interstitial grains between olivine and brown amphibole (Fig. 2c). The latter is classified as pargasite, suggesting a late-crystallising igneous phase (e.g., Féménias et al., 2006).

Intercumulus melt evolution revealed by compositional variations in minerals

Chemical evolution of intercumulus melt is indicated by the occurrence of: (1) evolved interstitial minerals, such as amphibole, orthopyroxene and zircon, which are not in textural and chemical equilibrium with cumulus olivine and clinopyroxene; (2) a large compositional variation (e.g., Ti and REE) in the intercumulus amphibole. We used thermometric and chemometric equations of different minerals to constrain the variations in the compositions and temperatures of intercumulus melts in the Yanhu cumulates.

Calcic amphibole compositions alone can act as very effective thermometers with a precision of ± 30°C because TiO_2 in amphibole varies considerably with temperature (Fig. 7a; Putirka, 2016). Calcic amphibole compositions can also be used to estimate the major and trace element compositions of its equilibrium melts (Humphreys et al., 2019; Putirka, 2016; Zhang et al., 2017). Recent tests reaffirmed that calculated melt SiO_2 contents and temperatures using different calibrations are consistent and reasonable (Putirka, 2016; Erdmann et al., 2014). We used the empirical equations (Eqs. 5 and 10) of Putirka (2016) to calculate amphibole crystallisation temperatures and its equilibrium melt SiO_2 contents. The REE and Zr contents of amphibole equilibrium melts were calculated using partition coefficients from the multiple-regression model of Humphreys et al. (2019), which links trace-element partition coefficients to amphibole major-element chemistry. The calculated results indicate that the brown and green amphiboles crystallised from mafic to intermediate melts (SiO_2 = 50–65 wt.%) at 1040 °C to 940 °C, and from felsic melts (SiO_2 = 70–74 wt.%) at 900 °C to 860 °C, respectively (Table S6). The calculated La/Sm ratios of amphibole equilibrium melts increase exponentially with increasing SiO_2 (Fig. 9b).

444 The crystallisation temperature of clinopyroxene was calculated using a clinopyroxene-only
445 thermometer of Wang et al. (2021). The clinopyroxene equilibrium melt Zr contents were
446 calculated using the partition coefficients compiled by Bédard (2001). The calculated results
447 show that clinopyroxene crystallised from melts with a Zr content of 80–155 μg/g at ~1150 °C
448 (Fig. 9a). The Al-in-olivine thermometer based on the partitioning of Al between coexisting
449 olivine and spinel inclusions (Coogan et al., 2014) was used to estimate olivine crystallisation
450 temperatures of 1135–1275 °C (Table S4). The spinels in this study have a high Ti (0.04–0.11 apfu;
451 Table S5) that exceeds the thermometer calibration range (<0.025 apfu), but previous
452 Al-exchange studies noted that Ti contents of <0.32 apfu do not produce anomalous results
453 (Coogan et al., 2014; Heinonen et al., 2015; Jennings et al., 2019).

454 The melts in equilibrium with clinopyroxene and amphibole display a transition from
455 increasing to decreasing Zr with decreasing temperature (Fig. 9a). The low-temperature felsic
456 melts in equilibrium with green amphibole have sufficiently high Zr content to achieve zircon
457 saturation (Fig. 9a) if felsic melts have M ([Na + K + 2Ca]/[Al·Si], all in cation fraction) values of
458 1–2, which characterize most felsic rocks (Miller et al., 2003). This suggests the cotectic
459 crystallisation of zircon and green amphibole from the felsic intercumulus melts.

460 We further explore whether the late-stage saturation of zircon can reproduce a marked
461 inflection in Dy/Yb versus La/Sm trends defined by both amphibole and apatite. We can calculate
462 the variations (i.e., the arrows with scales in Fig. 7c and 8c) in these ratios of amphibole/apatite
463 that crystallised from the intercumulus melts variably evolving from more primitive melts in
464 equilibrium with the earlier-crystallised amphibole/apatite. The intercumulus melt evolution was
465 modeled using fractional crystallisation of amphibole, apatite, and zircon, all of which are the

466 REE-rich intercumulus minerals in Yanhu ultramafic rocks. The partition coefficients (D) for these
467 minerals are assumed to be constant during the differentiation process and they are given in
468 Table S13. Although many experimental studies (e.g., Burnham and Berry, 2012; Prowatke and
469 Klemme, 2006; Tiepolo et al., 2007) have demonstrated that the absolute D_{REE} values vary
470 significantly with temperature and composition of melts, the D_{REE} ratios (e.g., $D_{La/Sm}$) are far less
471 prone to this problem (see below). The MREE (e.g., Sm, Dy) are more compatible than the HREE
472 (e.g., Yb) and LREE (e.g., La) in both amphibole and apatite (Prowatke and Klemme, 2006; Tiepolo
473 et al., 2007), but the HREE are more compatible than the MREE and LREE in zircon (Burnham and
474 Berry, 2012; Sano et al., 2002). In addition, F is more compatible than Cl in amphibole (Van den
475 Bleeken and Koga, 2015), fluorapatite, and hydroxyapatite (Li and Costa, 2020; McCubbin et al.,
476 2015). Therefore, the fractional crystallisation of amphibole and/or apatite can produce a
477 negative correlation between Cl/F and Dy/Yb in the residual melts and crystallising apatite (Fig.
478 8b).

479 The involvement of a small amount of zircon, along with amphibole and apatite, in the
480 fractionating mineral assemblages (e.g., amphibole, apatite, and zircon at a 90:9.7:0.3 ratio) can
481 buffer the decrease in Dy/Yb ratios that results from the fractionation of amphibole or apatite
482 alone (Fig. 7c and 8c). The proportion of zircon in the fractionating mineral assemblages depends
483 on the difference in absolute D_{REE} values of different minerals. The values along the curves with
484 scales in Fig. 7c and 8b–c denote the amount of fractionating minerals, but these values and
485 positions of curves are indicative only because they can vary with different choices of the
486 absolute D_{REE} values and starting compositions (i.e., black stars in Fig. 7c and 8 b–c), respectively.
487 However, these parameters do not significantly affect the slope of modeled curves, which were

488 determined by the D_{REE} ratios.

489 Brown amphibole in the Yanhu cumulates usually contains resorbed inclusions of
490 clinopyroxene and olivine, and some of the green amphiboles occur as replacive rims of the
491 brown amphiboles (Fig. 2a–c), suggesting that brown and green amphiboles formed through
492 peritectic reactions consuming the precursors of olivine + clinopyroxene and of brown amphibole,
493 respectively. Amphibole–forming peritectic reactions are different from the pure fractional
494 crystallization (FC) model above (Klaver et al., 2018; Wang et al., 2022). To incorporate the
495 effects of peritectic resorption, we follow the approach of Klaver et al. (2018) and use the
496 two-stage assimilation-fractional crystallisation (AFC) processes to model dissolution and
497 precipitation processes. The first stage (AFC1) is the assimilation of olivine + clinopyroxene and
498 the crystallisation of brown amphibole + orthopyroxene + apatite, and the second stage (AFC2) is
499 the assimilation of brown amphibole and the crystallisation of green amphibole + apatite + zircon.
500 We also show the pure FC1 and FC2 models which correspond exactly with the AFC1 and AFC2
501 models with the assimilated to crystallised mass ratio (r) of zero, respectively. We calculated the
502 Dy/Yb and La/Sm ratios of melts in equilibrium with the intercumulus amphibole, orthopyroxene,
503 and apatite to compare melt compositions and AFC trends. The D_{REE} values of amphibole and
504 orthopyroxene are calculated using the parameterized models developed by Humphreys et al.
505 (2019) and Sun and Liang (2013), respectively. The D_{REE} values of apatite are the average values
506 determined in experiments (Prowatke and Klemme, 2006; Watson and Green, 1981), and hence
507 the errors (2σ), caused by the uncertainties of D_{REE} values, are shown for calculated Dy/Yb and
508 La/Sm of apatite equilibrium melts (Fig. 10). The model parameters are described in the caption
509 of Fig. 10 and Table S13.

The modeling results (Fig. 10) show that the AFC1 trends vary insignificantly with r values. This is because the olivine–clinopyroxene assimilant in the AFC1 model has low REE contents. In contrast, the assimilant of brown amphibole in the AFC2 model has high REE contents and Dy/Yb ratios (Table S13). The residual evolving melts show decreasing MREE and HREE contents due to the fractionation of amphibole, apatite, and zircon, and hence they are susceptible to the assimilation of brown amphibole. A low degree of assimilation can even lead to an increase in Dy/Yb of late-stage melts (Fig. 10). Therefore, both the crystallisation of zircon and the assimilation of brown amphibole can suppress a decrease in Dy/Yb of late-stage melts.

The peritectic reaction forming amphibole (clinopyroxene + olivine + mafic melt = amphibole + orthopyroxene + felsic melt) observed in our samples has been also reproduced by cooling-driven crystallisation experiments on a hydrous basalt (Ulmer et al., 2018). The amphiboles containing resorbed inclusions of clinopyroxene and olivine can be the crystallisation products of hydrous basalts in a closed system, which does not necessarily require externally derived evolved melts in an open system. Combined with the calculated temperatures above, the main mineral crystallisation sequence is as follows: (1) minerals formed during cumulus processes: olivine + spinel, clinopyroxene; (2) minerals formed during postcumulus processes: brown amphibole + orthopyroxene + apatite, green amphibole + apatite + zircon. The Yanhu apatite crystallised earlier at a lower SiO_2 content than zircon, consistent with both the solubility models (Harrison and Watson, 1984; Watson and Harrison, 1983) and inflections in the Zr- and P–SiO_2 arrays for global arc lavas (Lee and Bachmann, 2014).

The effect of trapped liquid shift on cumulus olivine Fo values

532 Postcumulus diffusive re-equilibration between cumulus olivine and intercumulus evolved
533 melts is ubiquitous during solidification of trapped intercumulus liquids in orthocumulates from
534 mafic-ultramafic intrusions (e.g., Barnes, 1986; Yang et al., 2019). The change in composition of a
535 mineral (e.g., olivine) from that of the initially precipitated cumulus crystals to the final
536 composition after complete solidification is termed the "trapped liquid shift", which can
537 significantly reduce olivine Fo values. The extent of reduction is positively correlated with the
538 initial trapped melt fraction (TMF; Barnes, 1986; Yang et al., 2019). For example, crystallisation of
539 30% trapped liquid can lead to shifts of up to 10 mol% in Fo values (Barnes, 1986).

540 The Yanhu whole-rock cumulate compositions are envisaged to be the sum of the
541 composition of cumulus phases (olivine and clinopyroxene) and intercumulus melt (crystallised
542 as amphibole, orthopyroxene and accessory phases) trapped between them in a closed system.
543 Based on this mass balance model, Bedard (1994) proposed an equilibrium distribution method
544 (EDM) to constrain the TMF, assuming that the cumulus minerals are initially in equilibrium with
545 the trapped melt and no significant melt migration has occurred. When the composition of initial
546 trapped melt in equilibrium with cumulus minerals is known, it is possible to estimate the TMF.
547 Modelling results for the Yanhu cumulates are shown in Fig. 11, where we report the REE
548 patterns of clinopyroxene calculated assuming various amounts of TMF (5, 10, 20 and 30%) (see
549 the caption of Fig. 11 for more details). The composition of calculated clinopyroxene is sensitive
550 to the TMF, and REE enrichment in clinopyroxene tends to decrease at increasing amount of
551 trapped melt. If the composition of the melt in equilibrium with the cumulus clinopyroxene
552 included in brown amphibole represents that of the initial trapped melt, the REE pattern of
553 clinopyroxene computed assuming 10–20% of TMF is very similar to that of clinopyroxene.

554 However, TMF should be underestimated because the incompatible REE abundances in the
555 cumulus clinopyroxenes had been elevated by effects of the trapped liquid shift (Barnes, 1986;
556 Yang et al., 2019). If the composition of the coeval basalt at Yanhu reasonably represents the
557 initial composition of potential liquid entrapped in the cumulates, the clinopyroxene computed
558 assuming ~50% of TMF resembles that in equilibrium with the Yanhu basalt. In summary, a high
559 TMF (20–50%) can be expected in the Yanhu cumulates, which is consistent with the high
560 proportions (35–60%) of intercumulus phases (amphibole and orthopyroxene, Table S1). It
561 means a significant postcumulus compositional shift (about 10 mol%) in the Fo value of cumulus
562 olivine.

563 The effect of trapped liquid shift on olivine Fo values is further confirmed by the decoupling
564 of Al-in-olivine temperatures and olivine Fo values. We calculated the olivine liquidus of the
565 coeval high-MgO basalt at Yanhu using the Rhyolite-MELTS thermodynamic program (Gualda et
566 al., 2012) to show the real relationship between olivine crystallisation temperatures and Fo
567 values (Fig. 12a). Application of the barometric and hygrometric formulations developed by
568 Ridolfi et al. (2010) gives pressures of 269 ± 74 MPa and water contents of 4.0 ± 0.6 wt.% for the
569 amphiboles of Yanhu cumulates (Table S6), and hence calculations were performed at 0.1 and
570 0.3 GPa and assuming initial water contents of 4 wt.%. Aluminium is expected to diffuse much
571 more slowly in olivine than Mg and Fe (Spandler and O'Neill, 2010), and therefore Al-in-olivine
572 temperature is less susceptible to the trapped liquid shift compared to Fo values. The
573 Al-in-olivine temperatures (1135–1275°C) of Yanhu cumulates overlap with those of mid-ocean
574 ridge basalts (MORB; Coogan et al., (2014)) and liquidus temperatures of Yanhu primary basalts,
575 although olivine Fo values of the Yanhu cumulates are significantly lower (Fig. 12a). Thus, the

Yanhu olivine grains with crystallisation temperatures higher than 1200 °C can represent the first crystals (typically Fo = ~90) to crystallise from a primary mantle melt, but their Fo values had decreased by about 10 mol% after postcumulus diffusive exchange of Mg and Fe with the trapped evolved melts (Fig. 12a). This diffusion process is further supported by the low temperatures (646–754°C; Table S4) of Fe/Mg exchange between olivine and spinel, which were obtained using the thermometer of Ballhaus et al. (1991).

No contribution of crustal contamination to high-$\delta^{18}O$ zircon saturation

Zircon is a ubiquitous accessory mineral in felsic rocks (e.g., granitoids) because zircon solubility in silicate melts decreases exponentially with decreasing temperature (Watson and Harrison, 1983). Basaltic liquids require an unrealistically high abundance of >5000 μg/g Zr to directly crystallise zircon near the liquidus, and thus zircons found in mafic or ultramafic rocks (including our samples) should crystallise from late-stage, deeply evolved melts, likely of granitic composition, near the solidus (Boehnke et al., 2013; Borisov and Aranovich, 2019). However, the addition of crustal Zr and Si to mafic magmas during the AFC process in an open system may promote zircon saturation (Guo et al., 2013; Wang et al., 2016). This zircon type formed in an open system involves the reworking of preexisting crustal rocks by mantle-derived magmas (Kemp et al., 2007). Crustal contamination may commence before and/or during zircon crystallisation, which can explain why late-crystallised zircons have significantly higher $\delta^{18}O$ and lower εHf values than early-crystallised mafic minerals (e.g., olivine and pyroxene) in some mafic-ultramafic rocks (Guo et al., 2013; Wang et al., 2016). Therefore, whether the Yanhu high-$\delta^{18}O$ zircons record periods dominated by crustal growth or reworking depends on the

598 contribution of crustal contamination to zircon saturation.

599 Fractional crystallisation in a closed system will increase the $\delta^{18}O$ values of residual melts
600 (M), but the $\delta^{18}O$ values of zircon (Zrn) that crystallised from variably evolved melts remains
601 approximately constant because the fractionation, $\Delta^{18}O$(M-Zrn), increases at nearly the same
602 rate as $\delta^{18}O$(M) (Valley et al., 2005). Zircon ($\delta^{18}O$ = 5.3 ± 0.6‰; 2SD) and olivine (Ol; $\delta^{18}O$ = 5.18 ±
603 0.28‰; 2SD) in normal mantle have indistinguishable $\delta^{18}O$ values, indicating that $\Delta^{18}O$(Zrn-Ol) is
604 close to zero at magmatic temperatures (Mattey et al. 1994; Valley et al. 1998). Thus, olivine that
605 crystallised from primary mantle melts should have $\delta^{18}O$ values similar to zircon that crystallised
606 from evolved melts formed by closed-system fractional crystallisation of primary melts. The
607 Yanhu olivines and zircons have similar $\delta^{18}O$ values (Fig. 5), suggesting no crustal contamination
608 during magma evolution from olivine to zircon crystallisation.

609 Oxygen isotopes are less sensitive to crustal contamination compared with radiogenic Nd
610 isotopes owing to the equally high abundance of O in magmas and possible crustal assimilants
611 (James, 1981). Apatite Nd isotopes can further determine whether crustal contamination
612 contributed to zircon saturation in the Yanhu cumulates, considering that the variations in REE
613 composition of apatites record those of intercumulus melts before and after zircon saturation.
614 The similar trends between Dy/Yb and La/Sm for apatite and amphibole suggest their
615 co-crystallisation from the same melt. A clear correlation ($La/Sm = 0.002\times\exp[0.1429\times SiO_2]$; R^2 =
616 0.88) between La/Sm and SiO_2 for the amphibole equilibrium melts (Fig. 9b and 13a) can be used
617 to estimate the SiO_2 contents of apatite equilibrium melts if the La/Sm ratios of apatite
618 equilibrium melts can be calculated using the appropriate D_{REE}. Although apatite/melt D_{La} and
619 D_{Sm} values increase by about an order of magnitude with increasing SiO_2 of the melt, the $D_{La/Sm}$

620 (0.54 ± 0.26; 2SD) ratios do not change significantly (Fig. 13a; Prowatke and Klemme, 2006;
621 Watson and Green, 1981). Hence, the $D_{La/Sm}$ ratios are assumed to be constant during the
622 differentiation process. The calculated results indicate that the SiO_2 contents of apatite
623 equilibrium melts increase from ~55 wt.% to ~70 wt.%, but apatite εNd(t) values remain almost
624 constant (Fig. 13b). Thus, apatite Nd isotopes suggest no contribution of crustal contamination to
625 high-$\delta^{18}O$ zircon saturation during the closed-system differentiation of mafic to felsic
626 intercumulus melts.

627 Al-in-olivine temperatures of the ultramafic cumulates record the liquidus temperatures of
628 high-Fo (~90) olivines crystallised from a primary mantle melt. Considering that diffusion rates of
629 oxygen in olivine are comparable to those of Al (Spandler and O'Neill, 2010), olivine $\delta^{18}O$ values
630 are also less susceptible to the trapped liquid shift compared to Fo values. Moreover, a
631 closed-system differentiation of mafic to felsic intercumulus melts implies that postcumulus
632 re-equilibration of olivine with the intercumulus melt, even if present, cannot modify olivine $\delta^{18}O$
633 values. Therefore, the $\delta^{18}O$ values of the Yanhu olivines with crystallisation temperatures higher
634 than 1200 °C can represent those of high-Fo (~90) olivines before the trapped liquid shift. The
635 horizontal trend between temperatures (1275–1135°C) and $\delta^{18}O$ values (6.3–7.1‰) for the
636 Yanhu olivines (Fig. 12b) precludes the possibility of crustal contamination during the earliest
637 stages of crystallisation of primary basalt. It means that parental magmas of the Yanhu
638 cumulates originated a high-$\delta^{18}O$ mantle.

639

640 **Possible connection between the Yanhu volcanic and plutonic rocks**

641 Amphibole-rich mafic–ultramafic rocks are widely found in subduction zones (e.g., Chang et

al., 2021; Smith, 2014; Tiepolo et al., 2012; Wang et al., 2019). This is because high H_2O contents in mafic arc magmas can cause the early crystallisation of pargasitic amphibole and suppress the crystallisation of plagioclase (Grove et al., 2003; Sisson and Grove, 1993; Ulmer et al., 2018). The negative correlations between Dy/Yb and SiO_2 from erupted lavas in modern subduction zones and Yanhu areas (Fig. 6c) also show that amphibole is an important mineral during differentiation of arc magma (Barber et al., 2021; Davidson et al., 2007). The fractionation of amphibole will more efficiently drive residual melt compositions to higher SiO_2 and promote calc-alkaline differentiation trends than that of plagioclase and pyroxene. This is because amphibole contains significantly less SiO_2. The amphibole-rich ultramafic cumulates are thought to form by the reaction between residual water-rich melts and earlier-formed mushes with a framework of clinopyroxene + olivine crystals during cooling of mafic magmas (Chang et al., 2021; Smith, 2014; Wang et al., 2019). Melt segregation from an amphibole-dominated mush is a manifestation of crustal differentiation, which may be important for the ultimate production of felsic rocks and of SiO_2-rich continental crust (Barber et al., 2021).

Calculated melts in equilibrium with the amphiboles in Yanhu cumulates define the ranges of Dy/Yb, La/Sm, and SiO_2, overlapping the coeval lavas (Fig. 6d and 9b), suggesting that these lavas may represent the intercumulus melts extracted from cumulates with different amounts of residual amphibole. The Yanhu felsic rocks and ultramafic cumulates formed at ca. 110 Ma have similar zircon Hf isotopes (Fig. 5a), indicating a negligible role for crustal contamination or melting in the formation of coeval felsic rocks. However, considering that the Yanhu rhyolites are characterized by significantly negative Eu anomalies and MREE-depleted "trough-like" patterns (Fig. 6b), we suggest that they were possibly extracted from a shallow mush with a framework of

664 amphibole + plagioclase crystals, rather than directly from the Yanhu ultramafic cumulates. The
665 lack of plagioclase in the Yanhu ultramafic cumulates also excludes a direct connection. The
666 parental magma constructing this shallow mush could be an andesitic melt possibly extracted
667 from a deeper mafic-ultramafic mush (e.g., the Yanhu ultramafic cumulates). This model is
668 consistent with the trans-crustal magma plumbing system described by Cashman et al. (2017).

669 The Dy/Yb variation of the coeval lavas in the extensive Early Cretaceous strata is mainly
670 controlled by amphibole fractionation (Fig. 6c). Thus, many of Early Cretaceous amphibole-rich
671 cumulates complementary to the extensive lavas are possibly not exposed because the coeval
672 volcanic strata east of Yanhu Town have not been significantly eroded (Fig. 1b). The outcrop of
673 ultramafic cumulates we observed may be a small part of the large intrusion. Many Early
674 Cretaceous batholiths are exposed west of Yanhu Town where the coeval volcanic strata have
675 been eroded (Fig. 1b). In short, the Yanhu ultramafic pluton is only one of the deep
676 amphibole-rich cumulates complementary to the extensive volcanic rocks. These igneous rocks
677 are the products of intra-crustal differentiation of magmas derived from high-$\delta^{18}O$ arc mantle,
678 and record crustal growth at their zircon crystallisation ages.

679

680 **Using zircon oxygen isotopes to distinguish between crustal growth and**
681 **reworking?**

682 Continental crust has been proposed to form predominantly in arc settings (e.g., Rudnick,
683 1995). As the worldwide dataset for oxygen isotopes of arc samples grows, evidence grows for
684 the presence of high-$\delta^{18}O$ (5.5–7.6‰) olivine crystals found in mantle-derived magmas (Martin
685 et al., 2011). These examples show that high-Fo (≥ 90) olivines have high-$\delta^{18}O$ values, which

cannot result from contamination by high-$\delta^{18}O$ crustal material, and therefore the mantle source itself must be enriched in ^{18}O (Martin et al., 2011). Given that oxygen is a major element, the significantly high $\delta^{18}O$ values (>7‰) observed in some arc olivine crystals from a mass balance standpoint may require unrealistically high amounts of slab-derived components in the mantle source. Therefore, arc olivine crystals with high $\delta^{18}O$ (>7‰) values are difficult to explain by a single-stage flux-melting process and require a ^{18}O pre-enriched mantle (e.g., previously fluxed forearc region) with which a high-$\delta^{18}O$ fluid has isotopically reacted, without melting, during a prolonged subduction history (Auer et al., 2009; Dorendorf et al., 2000; Martin et al., 2011). The Hf isotope ratios of modern island arc magmas worldwide are thought to be more representative of new crust being generated from the mantle than are magmas generated along active continental margins, which are more prone to shallow-level processes of crustal contamination (Dhuime et al., 2011). The εHf values (5.5–17.7, average = 13.2; Hao et al., 2022) in island arcs are on average lower than the present-day value for the depleted MORB mantle (εHf = 16.9; Griffin et al., 2000), primarily because of contributions from subducted sediments (Hao et al., 2022). In short, many arc igneous rocks (e.g., the Yanhu samples), contaminated at their mantle source by subducted sediments, may show "non-MORB-like" zircon O–Hf signatures. Determining the mass fractions of those high-$\delta^{18}O$ rocks that derive from the mantle and recycled crust are important to unravel their contribution to crustal growth.

The estimated amount of subducted sediments in the source mantle based on oxygen isotopes of arc magmas is mainly determined by the $\delta^{18}O$ values of subducted sediments. The $\delta^{18}O$ values of subducted sediments are dominated by the relative proportions of carbonate and siliciclastic sediments ($\delta^{18}O$ = 25–32 ‰ and 10–20 ‰, respectively; Eiler, 2001). In addition,

siliciclastic sediments have higher Hf (generally >4 μg/g) contents than carbonate-rich sediments (generally <2 μg/g; Plank and Langmuir, 1998). We calculated simple binary mixing between carbonate-rich or siliciclastic sediments and a depleted MORB mantle. We assume the $\delta^{18}O$ values of 30‰ and 15‰ and Hf contents of 1 μg/g and 5 μg/g for the subducted carbonate-rich and siliciclastic sediments, respectively. The average εHf value (+2) for global subducted sediments estimated by Chauvel et al. (2008) is used for the sediment end-member. Other parameters used in the mixing calculations are given in the caption of Fig. 14. The amounts of subducted sediments in the source mantle of Yanhu cumulates are estimated to be 4–12 wt% (Fig. 14). Other studies (Cornet et al., 2022; Couzinié et al., 2016) also draw the same conclusions that the maximum amount of source contamination to keep the composition of a basalt with $\delta^{18}O$ < 8‰ should not exceed 15%. It means that about 88–96% of the bulk mass of our samples are of mantle origin and thus represent new additions to the crust, although their high-$\delta^{18}O$ signatures come from recycled crustal materials.

The main source rocks from which detrital zircons are derived are felsic magmatic rocks, such as granitoids and their extrusive equivalents. The comparison of experimentally produced melts and cumulates with natural arc rocks shows that fractional crystallisation of mantle-derived magmas is likely to be the dominant process in the formation of arc granitoids, with crustal melting and or assimilation a necessary but secondary contributor (Jagoutz and Klein, 2018; Müntener and Ulmer, 2018). For example, amphibole-rich mafic–ultramafic cumulates and genetically related lavas widely found in subduction zones define Dy/Yb versus SiO_2 trends indicative of amphibole fractionation (Fig. 6c). The Yanhu felsic rocks and ultramafic cumulates formed at ca. 110 Ma are the products of intra-crustal differentiation of magmas derived from

high-$\delta^{18}O$ arc mantle. Thus, ca. 110 Ma zircons from the Yanhu magmatic rocks record true periods of crustal growth although they have high-$\delta^{18}O$ values. If these zircon grains are hosted in clastic sedimentary rocks, they should not be simply assigned to crustal reworking in detrital zircon-based crustal evolution models. Our study also shows that the combination of zircon and olivine oxygen isotopes for ultramafic to felsic rocks in a given arc is more effective than zircon data alone in evaluating the role of crustal growth vs. reworking during a magmatic episode.

We stress that our case for source contamination does not preclude other mechanisms, such as crustal contamination and melting, for the generation of high-$\delta^{18}O$ zircons, particularly for zircons with extremely high $\delta^{18}O$ values (>8‰). For example, pure sediment-derived granites in the Himalayan orogen have been shown to crystallise zircon with $\delta^{18}O$ values of 8–12‰ (Hopkinson et al., 2017). Dhuime et al. (2012) presented a compilation of 1376 detrital zircon $\delta^{18}O$ analyses, which is thought to represent the O isotope record available for Earth's continental crust. Twenty-six percent of the zircon analyses in Dhuime et al. (2012) have moderately high $\delta^{18}O$ values of 6.1–7.2‰, identical to the Yanhu zircons. However, Spencer et al. (2022) recently recognized the decoupling of oxygen isotopes of zircon in sedimentary and igneous rocks and concluded that the detrital zircon record is strongly biased to upper crustal rocks, especially sediment-derived granites from collisional belts, rather than providing a representative view of the entire crust. A corollary is that the mid-to lower-crustal rocks with moderately high $\delta^{18}O$ (e.g., 6.1–7.2‰) zircons are not fully represented in the detrital zircon record. Thus, these moderately high $\delta^{18}O$ zircons are not only quantitatively underestimated, but also attributed to crustal reworking in global models, and in turn incorrectly assigned to "ancient" crust growth (i.e. given by zircon Hf model ages) instead of "instantaneous" growth (i.e.

752 given by zircon U-Pb ages). Our case study, as well as other regional and global studies (e.g.,
753 Cornet et al., 2022), have demonstrated that source contamination of the mantle wedge by
754 slab-derived material plays an important role in imprinting ultramafic to felsic arc rocks with high
755 $\delta^{18}O$ compositions. Therefore, distinguishing between crustal growth and reworking simply using
756 zircon oxygen isotopes may be over-simplistic and may underestimate crustal growth over the
757 past 2.5 Ga (Cornet et al., 2022; Couzinié et al., 2016).
758

759 ## CONCLUSIONS

760 Geochemical evidence from the Yanhu high-$\delta^{18}O$ zircon-bearing ultramafic cumulates and
761 coeval lavas from a Cretaceous magmatic arc in southern Tibet offers a unique opportunity to
762 evaluate the role of crustal growth vs. reworking during this Cretaceous (110 ± 2 Ma) magmatic
763 episode. The cumulates mainly comprise olivine and amphibole. Zircon crystallisation during
764 differentiation of the intercumulus melts is evidenced by the marked inflections in both Zr versus
765 SiO_2 trends defined by amphibole and those in Dy/Yb versus La/Sm trends defined by amphibole
766 and apatite. Apatite εNd(t) values (2.4 ± 1.4) did not change significantly before and after zircon
767 crystallisation. Interstitial zircons have $\delta^{18}O$ (6.1–7.2‰) values similar to the earliest crystallised
768 olivine ($\delta^{18}O$ = 6.3–7.1‰) in the cumulates. The comparison of cumulates and genetically related
769 lavas shows that they were ultimately derived from high-$\delta^{18}O$ arc mantle, and crystallised zircon
770 during magma evolution controlled by amphibole-dominated fractionation, without involving
771 crustal contamination or melting. Thus, ca. 110 Ma zircons from the Yanhu magmatic rocks are
772 not products of crustal reworking, but crustal growth although they have high-$\delta^{18}O$ values.
773 Distinguishing between crustal growth and reworking simply using zircon oxygen isotope may be

774 over-simplistic and conceal recent crustal growth in global zircon-based crustal evolution models.

775

776 FUNDING

777 This study was supported by the National Natural Science Foundation of China (grants
778 42021002, 42002047 and 91855215), the Second Tibetan Plateau Scientific Expedition and
779 Research (STEP) (grant 2019QZKK0702), and the Strategic Priority Research Program (A) of the
780 Chinese Academy of Sciences (CAS; XDA2007030402). This is contribution No. IS-XXXX from
781 GIGCAS.

782

783 ACKNOWLEDGEMENTS

784 We acknowledge Professor Roberta Rudnick and an anonymous reviewer for constructive
785 comments and Professors Georg Zellmer and Jason Harvey for editorial handling. We are grateful
786 for discussion with Dr. Xiaobing Zhang.

787

788 REFERENCES

789 Armstrong, R. L. (1981). Radiogenic Isotopes - the Case for Crustal Recycling on a
790 near-Steady-State No-Continental-Growth Earth. Philosophical Transactions of the Royal
791 Society a-Mathematical Physical and Engineering Sciences 301, 443-472.
792 Arndt, N. T. (2013). The Formation and Evolution of the Continental Crust. Geochemical
793 Perspectives 2, 405-533.
794 Arndt, N. T. & Goldstein, S. L. (1987). Use and Abuse of Crust-Formation Ages. Geology 15,
795 893-895.
796 Auer, S., Bindeman, I., Wallace, P., Ponomareva, V. & Portnyagin, M. (2009). The origin of
797 hydrous, high-delta O-18 voluminous volcanism: diverse oxygen isotope values and high
798 magmatic water contents within the volcanic record of Klyuchevskoy volcano, Kamchatka,
799 Russia. Contributions to Mineralogy and Petrology 157, 209-230.
800 Ballhaus, C., Berry, R. & Green, D. (1991). High pressure experimental calibration of the
801 olivine-orthopyroxene-spinel oxygen geobarometer: implications for the oxidation state of
802 the upper mantle. Contributions to Mineralogy and Petrology 107, 27-40.

803 Barber, N. D., Edmonds, M., Jenner, F., Audetat, A. & Williams, H. (2021). Amphibole control on
804 copper systematics in arcs: Insights from the analysis of global datasets. Geochimica Et
805 Cosmochimica Acta 307, 192-211.
806 Barnes, S. J. (1986). The Effect of Trapped Liquid Crystallization on Cumulus Mineral
807 Compositions in Layered Intrusions. Contributions to Mineralogy and Petrology 93, 524-531.
808 Bedard, J. H. (1994). A Procedure for Calculating the Equilibrium Distribution of Trace-Elements
809 among the Minerals of Cumulate Rocks, and the Concentration of Trace-Elements in the
810 Coexisting Liquids. Chemical Geology 118, 143-153.
811 Bedard, J. H. (2001). Parental magmas of the Nain Plutonic Suite anorthosites and mafic
812 cumulates: a trace element modelling approach. Contributions to Mineralogy and Petrology
813 141, 747-771.
814 Bindeman, I. (2008). Oxygen Isotopes in Mantle and Crustal Magmas as Revealed by Single
815 Crystal Analysis. Reviews in Mineralogy & Geochemistry 69, 445-478.
816 Bindeman, I., Gurenko, A., Sigmarsson, O. & Chaussidon, M. (2008). Oxygen isotope
817 heterogeneity and disequilibria of olivine crystals in large volume Holocene basalts from
818 Iceland: Evidence for magmatic digestion and erosion of Pleistocene hyaloclastites.
819 Geochimica et Cosmochimica Acta 72, 4397-4420.
820 Bindeman, I. N., Eiler, J. M., Yogodzinski, G. M., Tatsumi, Y., Stern, C. R., Grove, T. L., Portnyagin,
821 M., Hoernle, K. & Danyushevsky, L. V. (2005). Oxygen isotope evidence for slab melting in
822 modem and ancient subduction zones. Earth and Planetary Science Letters 235, 480-496.
823 Boehnke, P., Watson, E. B., Trail, D., Harrison, T. M. & Schmitt, A. K. (2013). Zircon saturation
824 re-revisited. Chemical Geology 351, 324-334.
825 Borisov, A. & Aranovich, L. (2019). Zircon solubility in silicate melts: New experiments and
826 probability of zircon crystallization in deeply evolved basic melts. Chemical Geology 510,
827 103-112.
828 Broom-Fendley, S., Styles, M. T., Appleton, J. D., Gunn, G. & Wall, F. (2016). Evidence for
829 dissolution-reprecipitation of apatite and preferential LREE mobility in carbonatite-derived
830 late-stage hydrothermal processes. American Mineralogist 101, 596-611.
831 Burnham, A. D. & Berry, A. J. (2012). An experimental study of trace element partitioning
832 between zircon and melt as a function of oxygen fugacity. Geochimica et Cosmochimica
833 Acta 95, 196-212.
834 Cashman, K. V., Sparks, R. S. J. & Blundy, J. D. (2017). Vertically extensive and unstable magmatic
835 systems: a unified view of igneous processes. Science 355, eaag3055.
836 Chakraborty, S. (2010). Diffusion coefficients in olivine, wadsleyite and ringwoodite. Reviews in
837 mineralogy and geochemistry 72, 603-639.
838 Chang, J., Audetat, A. & Li, J. W. (2021). In situ Reaction-replacement Origin of Hornblendites in
839 the Early Cretaceous Laiyuan Complex, North China Craton, and Implications for its
840 Tectono-magmatic Evolution. Journal of Petrology 62.
841 Chauvel, C., Lewin, E., Carpentier, M., Arndt, N. T. & Marini, J. C. (2008). Role of recycled oceanic
842 basalt and sediment in generating the Hf-Nd mantle array. Nature Geoscience 1, 64-67.
843 Coogan, L. A., Saunders, A. D. & Wilson, R. N. (2014). Aluminum-in-olivine thermometry of
844 primitive basalts: Evidence of an anomalously hot mantle source for large igneous provinces.
845 Chemical Geology 368, 1-10.
846 Cornet, J., Laurent, O., Wotzlaw, J.-F., Antonelli, M. A., Otamendi, J., Bergantz, G. W. & Bachmann,

O. (2022). Reworking subducted sediments in arc magmas and the isotopic diversity of the continental crust: The case of the Ordovician Famatinian crustal section, Argentina. Earth and Planetary Science Letters 595, 117706.

Couzinié, S., Laurent, O., Moyen, J. F., Zeh, A., Bouilhol, P. & Villaros, A. (2016). Post-collisional magmatism: Crustal growth not identified by zircon Hf-O isotopes. Earth and Planetary Science Letters 456, 182-195.

Dan, W., Wang, Q., Wang, X. C., Liu, Y., Wyman, D. A. & Liu, Y. S. (2015). Overlapping Sr-Nd-Hf-O isotopic compositions in Permian mafic enclaves and host granitoids in Alxa Block, NW China: Evidence for crust-mantle interaction and implications for the generation of silicic igneous provinces. Lithos 230, 133-145.

Davidson, J., Turner, S., Handley, H., Macpherson, C. & Dosseto, A. (2007). Amphibole "sponge" in arc crust? Geology 35, 787-790.

Depaolo, D. J. (1981). Neodymium Isotopes in the Colorado Front Range and Crust-Mantle Evolution in the Proterozoic. Nature 291, 193-196.

Dhuime, B., Hawkesworth, C. & Cawood, P. (2011). When continents formed. Age (Ga) 3, 4.

Dhuime, B., Hawkesworth, C. J., Cawood, P. A. & Storey, C. D. (2012). A change in the geodynamics of continental growth 3 billion years ago. Science 335, 1334-1336.

Dorendorf, F., Wiechert, U. & Worner, G. (2000). Hydrated sub-arc mantle: a source for the Kluchevskoy volcano, Kamchatka/Russia. Earth and Planetary Science Letters 175, 69-86.

Eiler, J. M. (2001). Oxygen isotope variations of basaltic lavas and upper mantle rocks. *Stable Isotope Geochemistry* 43, 319-364.

Erdmann, S., Martel, C., Pichavant, M. & Kushnir, A. (2014). Amphibole as an archivist of magmatic crystallization conditions: problems, potential, and implications for inferring magma storage prior to the paroxysmal 2010 eruption of Mount Merapi, Indonesia. Contributions to Mineralogy and Petrology 167.

Féménias, O., Mercier, J.-C. C., Nkono, C., Diot, H., Berza, T., Tatu, M. & Demaiffe, D. (2006). Calcic amphibole growth and compositions in calc-alkaline magmas: Evidence from the Motru Dike Swarm (Southern Carpathians, Romania). American Mineralogist 91, 73-81.

Griffin, W. L., Pearson, N. J., Belousova, E., Jackson, S. E., van Achterbergh, E., O'Reilly, S. Y. & Shee, S. R. (2000). The Hf isotope composition of cratonic mantle: LAM-MC-ICPMS analysis of zircon megacrysts in kimberlites. Geochimica et Cosmochimica Acta 64, 133-147.

Grimes, C. B., John, B. E., Cheadle, M. J., Mazdab, F. K., Wooden, J. L., Swapp, S. & Schwartz, J. J. (2009). On the occurrence, trace element geochemistry, and crystallization history of zircon from in situ ocean lithosphere. Contributions to Mineralogy and Petrology 158, 757.

Grove, T. L., Elkins-Tanton, L. T., Parman, S. W., Chatterjee, N., Muntener, O. & Gaetani, G. A. (2003). Fractional crystallization and mantle-melting controls on calc-alkaline differentiation trends. Contributions to Mineralogy and Petrology 145, 515-533.

Gualda, G. A. R., Ghiorso, M. S., Lemons, R. V. & Carley, T. L. (2012). Rhyolite-MELTS: a Modified Calibration of MELTS Optimized for Silica-rich, Fluid-bearing Magmatic Systems. Journal of Petrology 53, 875-890.

Guo, F., Guo, J. T., Wang, C. Y., Fan, W. M., Li, C. W., Zhao, L., Li, H. X. & Li, J. Y. (2013). Formation of mafic magmas through lower crustal AFC processes - An example from the Jinan gabbroic intrusion in the North China Block. Lithos 179, 157-174.

Hao, H., Campbell, I. H. & Park, J. W. (2022). Nd-Hf isotopic systematics of the arc mantle and

their implication for continental crust growth. Chemical Geology 602.
Hao, L. L., Wang, Q., Wyman, D. A., Ou, Q., Dan, W., Jiang, Z. Q., Wu, F. Y., Yang, J. H., Long, X. P. & Li, J. (2016). Underplating of basaltic magmas and crustal growth in a continental arc: Evidence from Late Mesozoic intermediate-felsic intrusive rocks in southern Qiangtang, central Tibet. Lithos 245, 223-242.
Harlov, D. E. (2015). Apatite: A Fingerprint for Metasomatic Processes. Elements 11, 171-176.
Harrison, T. M. & Watson, E. B. (1984). The Behavior of Apatite during Crustal Anatexis - Equilibrium and Kinetic Considerations. Geochimica et Cosmochimica Acta 48, 1467-1477.
Hawkesworth, C., Dhuime, B., Pietranik, A., Cawood, P., Kemp, A. & Storey, C. (2010). The generation and evolution of the continental crust. Journal of the Geological Society 167, 229-248.
Hawkesworth, C. J. & Kemp, A. I. S. (2006). Using hafnium and oxygen isotopes in zircons to unravel the record of crustal evolution. Chemical Geology 226, 144-162.
Hawthorne, F. C., Oberti, R., Harlow, G. E., Maresch, W. V., Martin, R. F., Schumacher, J. C. & Welch, M. D. (2012). Nomenclature of the amphibole supergroup. American Mineralogist 97, 2031-2048.
Heinonen, J. S., Jennings, E. S. & Riley, T. R. (2015). Crystallisation temperatures of the most Mg-rich magmas of the Karoo LIP on the basis of Al-in-olivine thermometry. Chemical Geology 411, 26-35.
Hopkinson, T. N., Harris, N. B. W., Warren, C. J., Spencer, C. J., Roberts, N. M. W., Horstwood, M. S. A., Parrish, R. R. & EIMF. (2017). The identification and significance of pure sediment-derived granites. Earth and Planetary Science Letters 467, 57-63.
Hoskin, P. W. O. (2005). Trace-element composition of hydrothermal zircon and the alteration of Hadean zircon from the Jack Hills, Australia. Geochimica Et Cosmochimica Acta 69, 637-648.
Hoskin, P. W. O. & Schaltegger, U. (2003). The composition of zircon and igneous and metamorphic petrogenesis. Zircon 53, 27-62.
Hou, Z. Q., Duan, L. F., Lu, Y. J., Zheng, Y. C., Zhu, D. C., Yang, Z. M., Yang, Z. S., Wang, B. D., Pei, Y. R., Zhao, Z. D. & McCuaig, T. C. (2015). Lithospheric Architecture of the Lhasa Terrane and Its Control on Ore Deposits in the Himalayan-Tibetan Orogen. Economic Geology 110, 1541-1575.
Hu, W.-L., Wang, Q., Tang, G.-J., Zhang, X.-Z., Qi, Y., Wang, J., Ma, Y.-M., Yang, Z.-Y., Sun, P. & Hao, L.-L. (2022). Late Early Cretaceous magmatic constraints on the timing of closure of the Bangong–Nujiang Tethyan Ocean, Central Tibet. Lithos 416-417, 106648.
Huang, X. L., Niu, Y. L., Xu, Y. G., Chen, L. L. & Yang, Q. J. (2010). Mineralogical and Geochemical Constraints on the Petrogenesis of Post-collisional Potassic and Ultrapotassic Rocks from Western Yunnan, SW China. Journal of Petrology 51, 1617-1654.
Humphreys, M. C. S., Cooper, G. F., Zhang, J., Loewen, M., Kent, A. J. R., Macpherson, C. G. & Davidson, J. P. (2019). Unravelling the complexity of magma plumbing at Mount St. Helens: a new trace element partitioning scheme for amphibole. Contributions to Mineralogy and Petrology 174, 1-15.
Iizuka, T., Campbell, I. H., Allen, C. M., Gill, J. B., Maruyama, S. & Makoka, F. (2013). Evolution of the African continental crust as recorded by U-Pb, Lu-Hf and O isotopes in detrital zircons from modern rivers. Geochimica et Cosmochimica Acta 107, 96-120.
Isa, J., Kohl, I. E., Liu, M. C., Wasson, J. T., Young, E. D. & McKeegan, K. D. (2017). Quantification

of oxygen isotope SIMS matrix effects in olivine samples: Correlation with sputter rate. Chemical Geology 458, 14-21.

Jagoutz, O. & Klein, B. (2018). On the Importance of Crystallization-Differentiation for the Generation of Sio2-Rich Melts and the Compositional Build-up of Arc (and Continental) Crust. American Journal of Science 318, 29-63.

James, D. E. (1981). The Combined Use of Oxygen and Radiogenic Isotopes as Indicators of Crustal Contamination. Annual Review of Earth and Planetary Sciences 9, 311-344.

Jennings, E. S., Gibson, S. A. & Maclennan, J. (2019). Hot primary melts and mantle source for the Parana-Etendeka flood basalt province: New constraints from Al-in-olivine thermometry. Chemical Geology 529.

Johnson, E. R., Wallace, P. J., Granados, H. D., Manea, V. C., Kent, A. J. R., Bindeman, I. N. & Donegan, C. S. (2009). Subduction-related Volatile Recycling and Magma Generation beneath Central Mexico: Insights from Melt Inclusions, Oxygen Isotopes and Geodynamic Models. Journal of Petrology 50, 1729-1764.

Kemp, A. I., Hawkesworth, C. J., Foster, G. L., Paterson, B. A., Woodhead, J. D., Hergt, J. M., Gray, C. M. & Whitehouse, M. J. (2007). Magmatic and crustal differentiation history of granitic rocks from Hf-O isotopes in zircon. Science 315, 980.

Kemp, A. I. S., Hawkesworth, C. J., Paterson, B. A. & Kinny, P. D. (2006). Episodic growth of the Gondwana supercontinent from hafnium and oxygen isotopes in zircon. Nature 439, 580-583.

Klaver, M., Blundy, J. D. & Vroon, P. Z. (2018). Generation of arc rhyodacites through cumulate-melt reactions in a deep crustal hot zone: Evidence from Nisyros volcano. Earth and Planetary Science Letters 497, 169-180.

Krneta, S., Ciobanu, C. L., Cook, N. J., Ehrig, K. & Kontonikas-Charos, A. (2016). Apatite at Olympic Dam, South Australia: A petrogenetic tool. Lithos 262, 470-485.

Lee, C.-T. A. & Bachmann, O. (2014). How important is the role of crystal fractionation in making intermediate magmas? Insights from Zr and P systematics. Earth and Planetary Science Letters 393, 266-274.

Li, S. M., Wang, Q., Zhu, D. C., Stern, R. J., Cawood, P. A., Sui, Q. L. & Zhao, Z. D. (2018). One or Two Early Cretaceous Arc Systems in the Lhasa Terrane, Southern Tibet. Journal of Geophysical Research-Solid Earth 123, 3391-3413.

Li, W. R. & Costa, F. (2020). A thermodynamic model for F-Cl-OH partitioning between silicate melts and apatite including non-ideal mixing with application to constraining melt volatile budgets. Geochimica Et Cosmochimica Acta 269, 203-222.

Li W., Tan K. (1998). Signal mineral separate method and its significance in geotectonics: Taking apatite and zircon as examples. Geotectonica et Metallogenia 22, 83-86.

Li, X. H., Li, Z. X., Wingate, M. T. D., Chung, S. L., Liu, Y., Lin, G. C. & Li, W. X. (2006). Geochemistry of the 755 Ma Mundine Well dyke swarm, northwestern Australia: Part of a Neoproterozoic mantle superplume beneath Rodinia? Precambrian Research 146, 1-15.

Li, X. H., Liu, Y., Li, Q. L., Guo, C. H. & Chamberlain, K. R. (2009). Precise determination of Phanerozoic zircon Pb/Pb age by multicollector SIMS without external standardization. Geochemistry Geophysics Geosystems 10, 1-21.

Li, X. H., Long, W. G., Li, Q. L., Liu, Y., Zheng, Y. F., Yang, Y. H., Chamberlain, K. R., Wan, D. F., Guo, C. H., Wang, X. C. & Tao, H. (2010). Penglai Zircon Megacrysts: A Potential New Working

Reference Material for Microbeam Determination of Hf-O Isotopes and U-Pb Age. Geostandards and Geoanalytical Research 34, 117-134.

Li, X. H., Tang, G. Q., Gong, B., Yang, Y. H., Hou, K. J., Hu, Z. C., Li, Q. L., Liu, Y. & Li, W. X. (2013). Qinghu zircon: A working reference for microbeam analysis of U-Pb age and Hf and O isotopes. Chinese Science Bulletin 58, 4647-4654.

Lu, Y.-J., Hou, Z.-Q., Yang, Z.-M., Parra-Avila, L. A., Fiorentini, M., McCuaig, T. C. & Loucks, R. R. (2017). Terrane-scale porphyry Cu fertility in the Lhasa terrane, southern Tibet. Geological Survey of Western Australia, Record 6, 95-100.

Ludwig, K. R. (2003). User's manual for Isoplot 3.00: a geochronological toolkit for Microsoft Excel: Kenneth R. Ludwig.

Martin, E., Bindeman, I. & Grove, T. L. (2011). The origin of high-Mg magmas in Mt Shasta and Medicine Lake volcanoes, Cascade Arc (California): higher and lower than mantle oxygen isotope signatures attributed to current and past subduction. Contributions to Mineralogy and Petrology 162, 945-960.

Mattey, D., Lowry, D. & Macpherson, C. (1994). Oxygen-Isotope Composition of Mantle Peridotite. Earth and Planetary Science Letters 128, 231-241.

McCubbin, F. M., Vander Kaaden, K. E., Tartese, R., Boyce, J. W., Mikhail, S., Whitson, E. S., Bell, A. S., Anand, M., Franchi, I. A., Wang, J. H. & Hauri, E. H. (2015). Experimental investigation of F, Cl, and OH partitioning between apatite and Fe-rich basaltic melt at 1.0-1.2 GPa and 950-1000 degrees C. American Mineralogist 100, 1790-1802.

Mcculloch, M. T. & Wasserburg, G. J. (1978). Sm-Nd and Rb-Sr Chronology of Continental Crust Formation. Science 200, 1003-1011.

Miller, C. F., McDowell, S. M. & Mapes, R. W. (2003). Hot and cold granites? Implications of zircon saturation temperatures and preservation of inheritance. Geology 31, 529-532.

Moyen, J.-F., Laurent, O., Chelle-Michou, C., Couzinié, S., Vanderhaeghe, O., Zeh, A., Villaros, A. & Gardien, V. (2017). Collision vs. subduction-related magmatism: two contrasting ways of granite formation and implications for crustal growth. Lithos 277, 154-177.

Muntener, O. & Ulmer, P. (2018). Arc Crust Formation and Differentiation Constrained by Experimental Petrology. American Journal of Science 318, 64-89.

Payne, J. L., McInerney, D. J., Barovich, K. M., Kirkland, C. L., Pearson, N. J. & Hand, M. (2016). Strengths and limitations of zircon Lu-Hf and O isotopes in modelling crustal growth. Lithos 248, 175-192.

Pettke, T., Audétat, A., Schaltegger, U. & Heinrich, C. A. (2005). Magmatic-to-hydrothermal crystallization in the W–Sn mineralized Mole Granite (NSW, Australia): Part II: Evolving zircon and thorite trace element chemistry. Chemical Geology 220, 191-213.

Plank, T. & Langmuir, C. H. (1998). The chemical composition of subducting sediment and its consequences for the crust and mantle. Chemical Geology 145, 325-394.

Prowatke, S. & Klemme, S. (2006). Trace element partitioning between apatite and silicate melts. Geochimica et Cosmochimica Acta 70, 4513-4527.

Putirka, K. (2016). Amphibole thermometers and barometers for igneous systems and some implications for eruption mechanisms of felsic magmas at arc volcanoes. American Mineralogist 101, 841-858.

Ridolfi, F., Renzulli, A. & Puerini, M. (2010). Stability and chemical equilibrium of amphibole in calc-alkaline magmas: an overview, new thermobarometric formulations and application to

subduction-related volcanoes. Contributions to Mineralogy and Petrology 160, 45-66.
Roberts, N. M. & Spencer, C. J. (2015). The zircon archive of continent formation through time. Geological Society, London, Special Publications 389, 197-225.
Rudnick, R. L. (1995). Making Continental-Crust. Nature 378, 571-578.
Sano, Y., Terada, K. & Fukuoka, T. (2002). High mass resolution ion microprobe analysis of rare earth elements in silicate glass, apatite and zircon: lack of matrix dependency. Chemical Geology 184, 217-230.
Sisson, T. W. & Grove, T. L. (1993). Experimental investigations of the role of H2O in calc-alkaline differentiation and subduction zone magmatism. Contributions to Mineralogy and Petrology 113, 143-166.
Sláma, J., Kosler, J., Condon, D. J., Crowley, J. L., Gerdes, A., Hanchar, J. M., Horstwood, M. S. A., Morris, G. A., Nasdala, L., Norberg, N., Schaltegger, U., Schoene, B., Tubrett, M. N. & Whitehouse, M. J. (2008). Plesovice zircon - A new natural reference material for U-Pb and Hf isotopic microanalysis. Chemical Geology 249, 1-35.
Smith, D. J. (2014). Clinopyroxene precursors to amphibole sponge in arc crust. Nature Communications 5, 4329.
Spandler, C. & O'Neill, H. S. (2010). Diffusion and partition coefficients of minor and trace elements in San Carlos olivine at 1,300A degrees C with some geochemical implications. Contributions to Mineralogy and Petrology 159, 791-818.
Spencer, C. J., Cavosie, A. J., Morrell, T. R., Lu, G. M., Liebmann, J. & Roberts, N. M. W. (2022). Disparities in oxygen isotopes of detrital and igneous zircon identify erosional bias in crustal rock record. Earth and Planetary Science Letters 577, 117248.
Sui, Q. L., Wang, Q., Zhu, D. C., Zhao, Z. D., Chen, Y., Santosh, M., Hu, Z. C., Yuan, H. L. & Mo, X. X. (2013). Compositional diversity of ca. 110 Ma magmatism in the northern Lhasa Terrane, Tibet: Implications for the magmatic origin and crustal growth in a continent-continent collision zone. Lithos 168, 144-159.
Sun, C. G. & Liang, Y. (2013). Distribution of REE and HFSE between low-Ca pyroxene and lunar picritic melts around multiple saturation points. Geochimica Et Cosmochimica Acta 119, 340-358.
Sun, S.-S. & McDonough, W. F. (1989). Chemical and isotopic systematics of oceanic basalts: implications for mantle composition and processes. Geological Society, London, Special Publications 42, 313-345.
Tang, G. Q., Su, B. X., Li, Q. L., Xia, X. P., Jing, J. J., Feng, L. J., Martin, L., Yang, Q. & Li, X. H. (2019). High-Mg# Olivine, Clinopyroxene and Orthopyroxene Reference Materials for In Situ Oxygen Isotope Determination. Geostandards and Geoanalytical Research 43, 585-593.
Tiepolo, M., Langone, A., Morishita, T. & Yuhara, M. (2012). On the recycling of amphibole-rich ultramafic intrusive rocks in the arc crust: evidence from Shikanoshima Island (Kyushu, Japan). Journal of Petrology 53, 1255-1285.
Tiepolo, M., Oberti, R., Zanetti, A., Vannucci, R. & Foley, S. F. (2007). Trace-element partitioning between amphibole and silicate melt. Reviews in mineralogy and geochemistry 67, 417-452.
Ulmer, P., Kaegi, R. & Müntener, O. (2018). Experimentally Derived Intermediate to Silica-rich Arc Magmas by Fractional and Equilibrium Crystallization at 1.0 GPa: an Evaluation of Phase Relationships, Compositions, Liquid Lines of Descent and Oxygen Fugacity. Journal of Petrology 59, 11-58.

1067 Valley, J. W., Kinny, P. D., Schulze, D. J. & Spicuzza, M. J. (1998). Zircon megacrysts from
1068 kimberlite: oxygen isotope variability among mantle melts. Contributions to Mineralogy and
1069 Petrology 133, 1-11.
1070 Valley, J. W., Lackey, J. S., Cavosie, A. J., Clechenko, C. C., Spicuzza, M. J., Basei, M. A. S.,
1071 Bindeman, I. N., Ferreira, V. P., Sial, A. N. & King, E. M. (2005). 4.4 billion years of crustal
1072 maturation: oxygen isotope ratios of magmatic zircon. Contributions to Mineralogy and
1073 Petrology 150, 561-580.
1074 Van den Bleeken, G. & Koga, K. T. (2015). Experimentally determined distribution of fluorine and
1075 chlorine upon hydrous slab melting, and implications for F-Cl cycling through subduction
1076 zones. Geochimica Et Cosmochimica Acta 171, 353-373.
1077 Wang, J., Wang, Q., Dan, W., Yang, J.-H., Yang, Z.-Y., Sun, P., Qi, Y. & Hu, W.-L. (2019). The role of
1078 clinopyroxene in amphibole fractionation of arc magmas: Evidence from mafic intrusive
1079 rocks within the Gangdese arc, southern Tibet. Lithos 338-339, 174-188.
1080 Wang, J., Wang, Q., Zeng, J.-P., Ou, Q., Dan, W., Yang, Y., Alexandra, Chen, Y.-W. & Wei, G. (2022).
1081 Generation of continental alkalic mafic melts by tholeiitic melt-mush reactions: A new
1082 perspective from contrasting mafic cumulates and dikes in central Tibet. Journal of
1083 Petrology 63, 1-21.
1084 Wang, M. X., Nebel, O. & Wang, C. Y. (2016). The Flaw in the Crustal 'Zircon Archive': Mixed Hf
1085 Isotope Signatures Record Progressive Contamination of Late-stage Liquid in
1086 Mafic-Ultramafic Layered Intrusions. Journal of Petrology 57, 27-52.
1087 Wang, X. D., Hou, T., Wang, M., Zhang, C., Zhang, Z. C., Pan, R. H., Marxer, F., Zhang, H. L. (2021).
1088 A new clinopyroxene thermobarometer for mafic to intermediate magmatic systems.
1089 European Journal of Mineralogy 33, 621-637.
1090 Wasserburg, G. J., Jacobsen, S. B., Depaolo, D. J., McCulloch, M. T. & Wen, T. (1981). Precise
1091 Determination of Sm/Nd Ratios, Sm and Nd Isotopic Abundances in Standard Solutions.
1092 Geochimica et Cosmochimica Acta 45, 2311-2323.
1093 Watson, E. B. & Green, T. H. (1981). Apatite Liquid Partition-Coefficients for the Rare-Earth
1094 Elements and Strontium. Earth and Planetary Science Letters 56, 405-421.
1095 Watson, E. B. & Harrison, T. M. (1983). Zircon Saturation Revisited - Temperature and
1096 Composition Effects in a Variety of Crustal Magma Types. Earth and Planetary Science
1097 Letters 64, 295-304.
1098 Weis, D., Kieffer, B., Maerschalk, C., Pretorius, W. & Barling, J. (2005). High-precision Pb-Sr-Nd-Hf
1099 isotopic characterization of USGS BHVO-1 and BHVO-2 reference materials. Geochemistry
1100 Geophysics Geosystems 6, Q02002.
1101 Wenner, D. B. & Taylor, H. P. (1971). Temperatures of Serpentinization of Ultramafic Rocks Based
1102 on O18/O16 Fractionation between Coexisting Serpentine and Magnetite. Contributions to
1103 Mineralogy and Petrology 32, 165-185.
1104 Wu, F. Y., Yang, Y. H., Xie, L. W., Yang, J. H. & Xu, P. (2006). Hf isotopic compositions of the
1105 standard zircons and baddeleyites used in U-Pb geochronology. Chemical Geology 234,
1106 105-126.
1107 Yang, Q., Xia, X., Zhang, W., Zhang, Y., Xiong, B., Xu, Y., Wang, Q. & Wei, G. (2018). An evaluation
1108 of precision and accuracy of SIMS oxygen isotope analysis. Solid Earth Sciences 3, 81-86.
1109 Yang, Y. H., Wu, F. Y., Yang, J. H., Chew, D. M., Xie, L. W., Chu, Z. Y., Zhang, Y. B. & Huang, C.
1110 (2014). Sr and Nd isotopic compositions of apatite reference materials used in U-Th-Pb

geochronology. Chemical Geology 385, 35-55.
Zeng, Y. C., Xu, J. F., Huang, F., Li, M. J. & Chen, Q. (2020). Generation of the 105-100 Ma Dagze volcanic rocks in the north Lhasa Terrane by lower crustal melting at different temperature and depth: Implications for tectonic transition. Geological Society of America Bulletin 132, 1257-1272.
Zhang, J., Humphreys, M. C. S., Cooper, G. F., Davidson, J. P. & Macpherson, C. G. (2017). Magma mush chemistry at subduction zones, revealed by new melt major element inversion from calcic amphiboles. American Mineralogist 102, 1353-1367.
Zhang, L., Ren, Z.-Y., Xia, X.-P., Yang, Q., Hong, L.-B. & Wu, D. (2019). In situ determination of trace elements in melt inclusions using laser ablation inductively coupled plasma sector field mass spectrometry. Rapid Communications in Mass Spectrometry 33, 361-370.
Zhang, L., Wu, J. L., Zhang, Y. Q., Yang, Y. N., He, P. L., Xia, X. P. & Ren, Z. Y. (2021). Simultaneous determination of Sm-Nd isotopes, trace-element compositions and U-Pb ages of titanite using a laser-ablation split-stream technique with the addition of water vapor. Journal of Analytical Atomic Spectrometry 36, 2312-2321.
Zhang, X. B., Guo, F., Zhang, B., Zhao, L., Wu, Y. M., Wang, G. Q. & Alemayehu, M. (2020). Magmatic evolution and post-crystallization hydrothermal activity in the early Cretaceous Pingtan intrusive complex, SE China: records from apatite geochemistry. Contributions to Mineralogy and Petrology 175.
Zhu, D.-C., Zhao, Z.-D., Niu, Y., Mo, X.-X., Chung, S.-L., Hou, Z.-Q., Wang, L.-Q. & Wu, F.-Y. (2011). The Lhasa Terrane: Record of a microcontinent and its histories of drift and growth. Earth and Planetary Science Letters 301, 241-255.

FIGURE CAPTIONS

Fig. 1. (a) Contour map of zircon εHf values for the Mesozoic-Cenozoic granitoid rocks and felsic volcanic rocks in the Lhasa terrane (modified from Lu et al., (2017)). (b) Simplified geological map showing the spatial distributions of Early Cretaceous magmatism in the northern Lhasa subterrane (Li et al., 2018). Ages for ca. 110 Ma magmatic rocks in the Yanhu area are from Zhu et al. (2011) and Sui et al. (2013). (c) Geological map showing the location of Yanhu ultramafic cumulates.

Fig. 2. Photomicrographs of the Yanhu cumulates. (a–c) Spatially separated but optically continuous amphibole grains enclosing olivine and clinopyroxene of rounded and irregular

1144 shapes. (d) An intercumulus orthopyroxene with olivine inclusions. (e) Two zircon grains in
1145 phlogopite. (f) Olivine, clinopyroxene, and apatite as inclusions in a large amphibole oikocryst. (g)
1146 Apatite as a late interstitial phase between orthopyroxene and amphibole. The olivine (d) and
1147 clinopyroxene (f) inclusions have embayed rims that are outlined by the white line. Note that
1148 (a–c) and (d–e) were under plane- and cross-polarized light, respectively, and (f–g) are BSE
1149 images. Abbreviations: Amp = amphibole, Ol = olivine, Opx = orthopyroxene, Cpx = clinopyroxene,
1150 Phl = phlogopite, Ap = apatite, Zrn = zircon, and Ser = serpentine.
1151
1152 **Fig. 3.** Representative BSE images of olivine with spinel inclusions (a) and apatite (b) in the Yanhu
1153 cumulates. The EPMA, LA–ICP–MS, SIMS, and LA–MC–ICP–MS spots for major and trace
1154 elements and O and Nd isotopes are marked with circles of different colours, respectively, and
1155 representative results are shown near the grains.
1156
1157 **Fig. 4.** SIMS zircon U–Pb concordia diagram (a–b) with representative zircon CL images (c–d) for
1158 the Yanhu cumulates. The spots for chemical analyses are marked on the grains and the numbers
1159 below the grains are $^{206}Pb/^{238}U$ ages at the top, εHf(t) value at the bottom left and $\delta^{18}O$ value at
1160 the bottom right. The data for spots with grey ellipses are excluded in the calculation of the
1161 weighted ages.
1162
1163 **Fig. 5.** (a) Zircon $\delta^{18}O$ vs. εHf(t). Also shown for comparison are the histograms of zircon εHf(t)
1164 values for the Yanhu felsic rocks formed at 110 ± 2 Ma (Sui et al., 2013; Zhu et al., 2011). (b)
1165 Olivine $\delta^{18}O$ vs. Fo. Gray shaded area represents $\delta^{18}O$ values of normal mantle zircon and olivine

(Mattey et al. 1994; Valley et al. 1998). Error bars are 2σ for $\delta^{18}O$ values.

Fig. 6. Major- and trace-element compositions of ultramafic cumulates in this study and basalts, andesites, rhyolites, and diorites reported by Sui et al. (2013). (a) MgO vs. SiO_2. (b) Chondrite-normalized REE patterns. Normalizing values are from Sun and McDonough (1989) (c) Dy/Yb vs. SiO_2. The data for several active arc volcanoes are from Davidson et al. (2007), which define differentiation trends indicative of amphibole fractionation. The inset shows the effect of fractionation of garnet, amphibole, and gabbro (pyroxene + plagioclase + olivine) on magma compositions (after Davidson et al. (2007)). (d) Dy/Yb vs. La/Sm. Calculated melts in equilibrium with amphiboles in Yanhu cumulates are shown for comparison.

Fig. 7. Major- and trace-element compositions of amphibole in the Yanhu cumulates. (a) TiO_2 vs. SiO_2. (b) Chondrite-normalized REE patterns. Clinopyroxene inclusions in brown amphibole are plotted for comparison. Normalizing values are from Sun and McDonough (1989). (c) Dy/Yb vs. La/Sm. Arrows with scales indicate the compositional variations of amphiboles resulting from the fractionation of different minerals from their equilibrium melts. Numbers along the arrows denote the amount of fractionating minerals. Mineral abbreviations are the same as in Fig. 2. The black stars represent the starting compositions. (d) Zr vs. SiO_2. All data points in (a), (c) and (d) are colour-coded for amphibole crystallisation temperatures obtained from Eq. 5 of Putirka (2016), with the scale displayed in (a).

Fig. 8. Major- and trace-element compositions of apatite in the Yanhu cumulates. (a) ΣREE vs. Cl.

(b) Dy/Yb vs. Cl/F. (c) Dy/Yb vs. La/Sm. Arrows with scales are the same as those in Fig. 7(c), except that the starting compositions (i.e., black stars) are different. (d) εNd(t) vs. La/Sm. Also shown for comparison are the whole-rock εNd(t) values.

Fig. 9. (a) The crystallisation temperatures of amphibole and clinopyroxene vs. their equilibrium melt Zr contents. Solubility of zircon as function of temperature and melt composition (M = [Na + K + 2Ca]/[Al·Si]) is from Watson and Harrison (1983). (b) La/Sm vs. SiO_2 for amphibole equilibrium melts showing the best-fit line. Error bars are 1σ for the calculated temperatures and SiO_2 contents.

Fig. 10. Geochemical models reproducing the variations in Dy/Yb and La/Sm ratios of the calculated melts in equilibrium with amphibole, orthopyroxene, and apatite. See text for model details and input parameters are given in Table S13. The AFC1 and AFC2 models are performed assuming the following peritectic reactions: Melt1 + 0.89 Ol + 0.11 Cpx = Melt2 + 0.8 Brown Amp + 0.16 Opx + 0.04 Ap (r= 0.6), Melt2 + Brown Amp = Melt3 + 0.9 Green Amp + 0.097 Ap + 0.003 Zrn (r = 0.1, 0.2, 0.3), respectively. The proportions of the assimilated (Ol : Cpx = 8:1) and crystallised (Brown Amp : Opx = 5:1) minerals are assumed based on the modal mineral proportions in thin sections (Table S1). The pure FC1 and FC2 models correspond exactly with the AFC1 and AFC2 models with r = 0, respectively. Errors (2σ) incorporate the uncertainties of D_{REE} values of apatite. Crosses on the modeled curves indicate 10% changes in the fraction of melt remaining.

Fig. 11. Chondrite-normalized REE abundances of clinopyroxenes calculated with the method of Bedard (1994) and (2001) assuming the trapped melt fractions (TMF) of 5, 10, 20, 30 and 50%. The proportion of the initial cumulus phases (olivine : clinopyroxene = 8:1) is assumed for all TMF based on the modal mineral proportions in thin sections (Table S1). We used the average abundances of cumulates and crystal/melt partition coefficients from Bedard (2001). The REE pattern of clinopyroxene in equilibrium with a Yanhu high-MgO basalt (YH22-2; Sui et al., 2013) are also reported for comparison.

Fig. 12. Al-in-olivine temperature vs. olivine Fo (a) and olivine $\delta^{18}O$ values (b). Two red curves show the olivine liquidus of a Yanhu high-MgO basalt (YH22-2; Sui et al., 2013) at 0.1 and 0.3 GPa, which were obtained using Rhyolite-MELTS (Gualda et al., 2012). The Al-in-olivine temperatures of MORB are from Coogan et al. (2014).

Fig. 13. (a) Apatite/melt D_{REE} and apatite equilibrium melt La/Sm ratios vs. apatite equilibrium melt SiO_2 contents. Experimentally determined D_{REE} values are from Prowatke and Klemme (2006) and Watson and Green (1981). (b) Apatite εNd(t) values vs. its equilibrium melt SiO_2 contents. Errors (2σ) for calculated SiO_2 contents of apatite equilibrium melts incorporate the uncertainties of apatite/melt $D_{La/Sm}$ (Fig. 13a) and predicted melt SiO_2 contents (Fig. 9b) from amphibole chemometry of Putirka (2016).

Fig. 14. Calculated $\delta^{18}O$ of mafic melts (from the measured $\delta^{18}O$ of zircon) vs. εHf(t). Also shown for comparison are the histograms of calculated $\delta^{18}O$ values for olivine equilibrium melts. The

1232 $\Delta^{18}O$(Melt-Zircon) and $\Delta^{18}O$(Melt-Olivine) fractionation factors were assumed to be 0.5‰ for
1233 mafic melts (Valley et al., 2005) and 0.7‰ for mafic melts at 1200°C (Eiler, 2001), respectively.
1234 Numbers along the green and purple curves of binary mixing denote the amounts of subducted
1235 sediments in the source mantle of Yanhu cumulates. The mantle end-member used in the mixing
1236 calculation: εHf(t = 110 Ma) = +16.5 (Griffin et al., 2000), Hf = 0.309 μg/g (Sun and McDonough,
1237 1989), $\delta^{18}O$ = 5.5 ± 0.2‰ (Eiler, 2001).

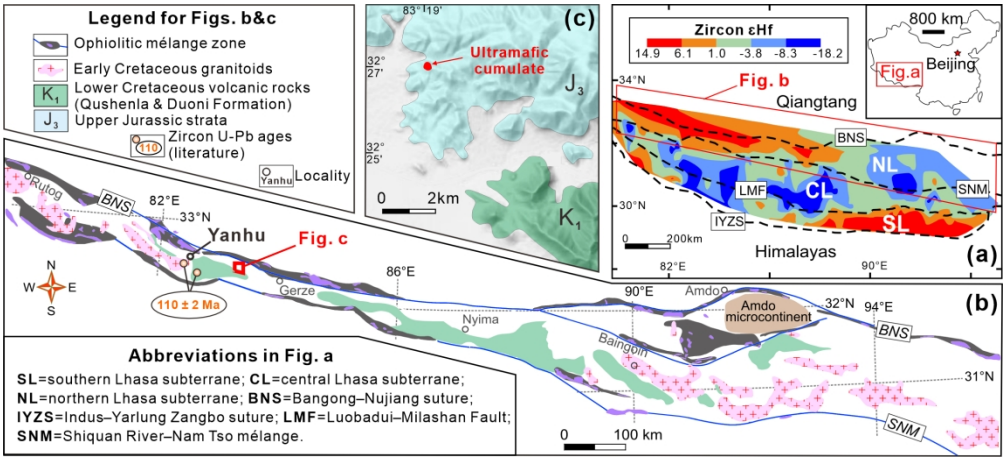

Fig. 1. (a) Contour map of zircon εHf values for the Mesozoic-Cenozoic granitoid rocks and felsic volcanic rocks in the Lhasa terrane (modified from Lu et al., (2017)). (b) Simplified geological map showing the spatial distributions of Early Cretaceous magmatism in the northern Lhasa subterrane (Li et al., 2018). Ages for ca. 110 Ma magmatic rocks in the Yanhu area are from Zhu et al. (2011) and Sui et al. (2013). (c) Geological map showing the location of Yanhu ultramafic cumulates.

191x86mm (300 x 300 DPI)

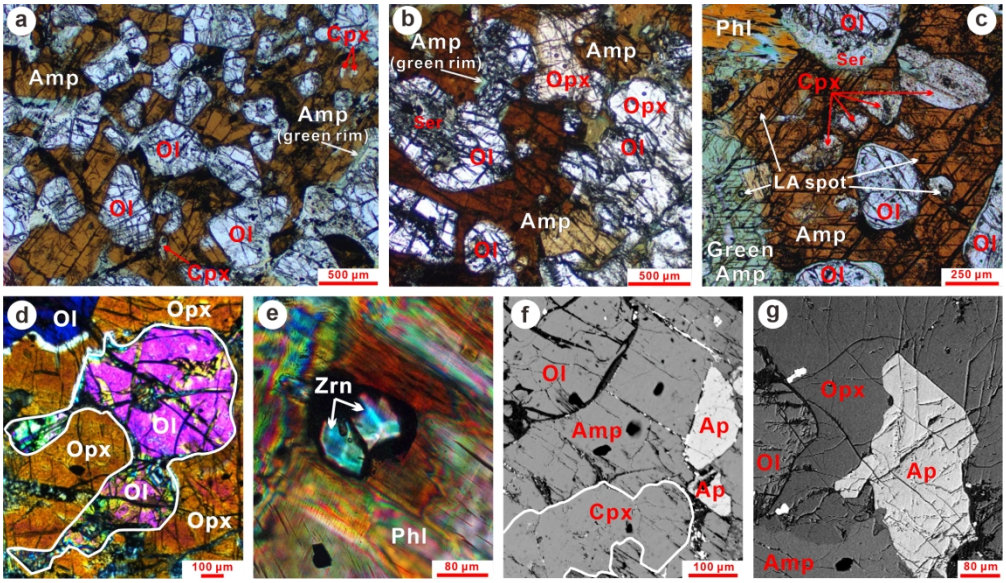

Fig. 2. Photomicrographs of the Yanhu cumulates. (a–c) Spatially separated but optically continuous amphibole grains enclosing olivine and clinopyroxene of rounded and irregular shapes. (d) An intercumulus orthopyroxene with olivine inclusions. (e) Two zircon grains in phlogopite. (f) Olivine, clinopyroxene, and apatite as inclusions in a large amphibole oikocryst. (g) Apatite as a late interstitial phase between orthopyroxene and amphibole. The olivine (d) and clinopyroxene (f) inclusions have embayed rims that are outlined by the white line. Note that (a–c) and (d–e) were under plane- and cross-polarized light, respectively, and (f–g) are BSE images. Abbreviations: Amp = amphibole, Ol = olivine, Opx = orthopyroxene, Cpx = clinopyroxene, Phl = phlogopite, Ap = apatite, Zrn = zircon, and Ser = serpentine.

194x112mm (300 x 300 DPI)

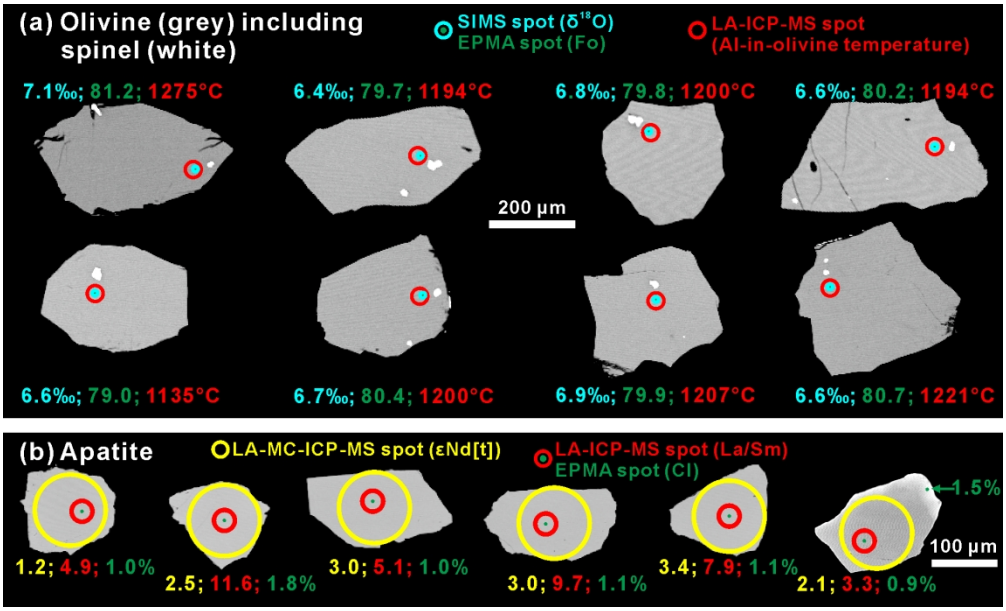

Fig. 3. Representative BSE images of olivine with spinel inclusions (a) and apatite (b) in the Yanhu cumulates. The EPMA, LA–ICP–MS, SIMS, and LA–MC–ICP–MS spots for major and trace elements and O and Nd isotopes are marked with circles of different colours, respectively, and representative results are shown near the grains.

169x102mm (300 x 300 DPI)

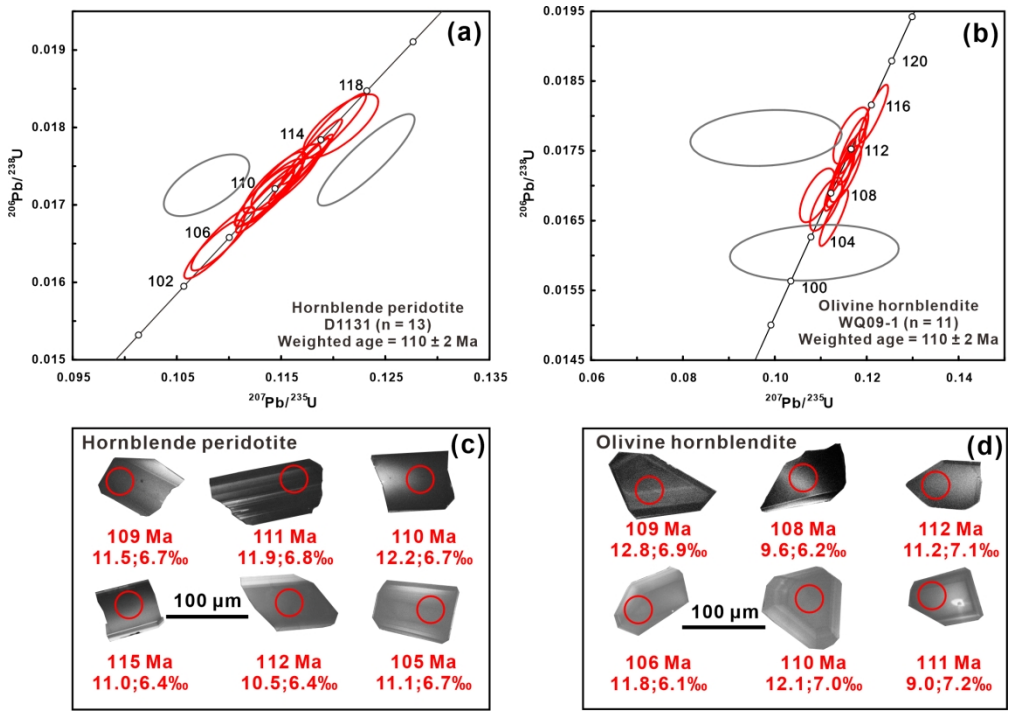

Fig. 4. SIMS zircon U–Pb concordia diagram (a–b) with representative zircon CL images (c–d) for the Yanhu cumulates. The spots for chemical analyses are marked on the grains and the numbers below the grains are 206Pb/238U ages at the top, εHf(t) value at the bottom left and δ18O value at the bottom right. The data for spots with grey ellipses are excluded in the calculation of the weighted ages.

186x131mm (300 x 300 DPI)

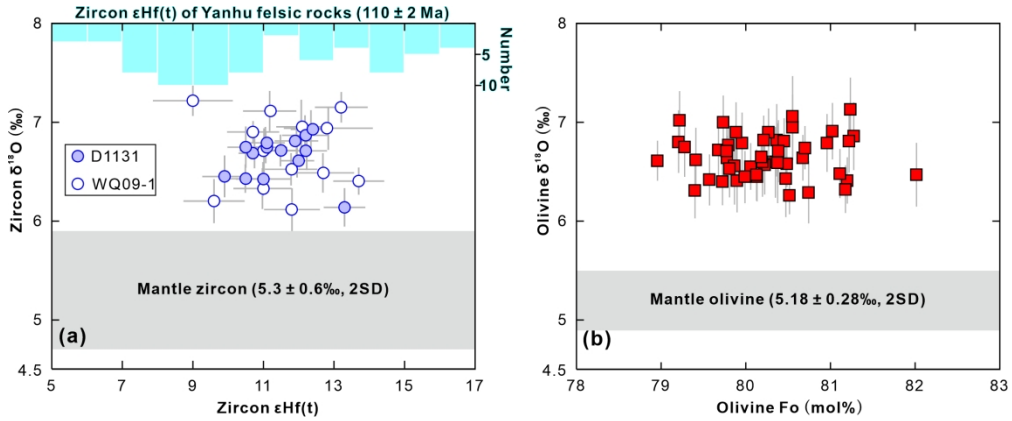

Fig. 5. (a) Zircon δ18O vs. εHf(t). Also shown for comparison are the histograms of zircon εHf(t) values for the Yanhu felsic rocks formed at 110 ± 2 Ma (Sui et al., 2013; Zhu et al., 2011). (b) Olivine δ18O vs. Fo. Gray shaded area represents δ18O values of normal mantle zircon and olivine (Mattey et al. 1994; Valley et al. 1998). Error bars are 2σ for δ18O values.

203x83mm (300 x 300 DPI)

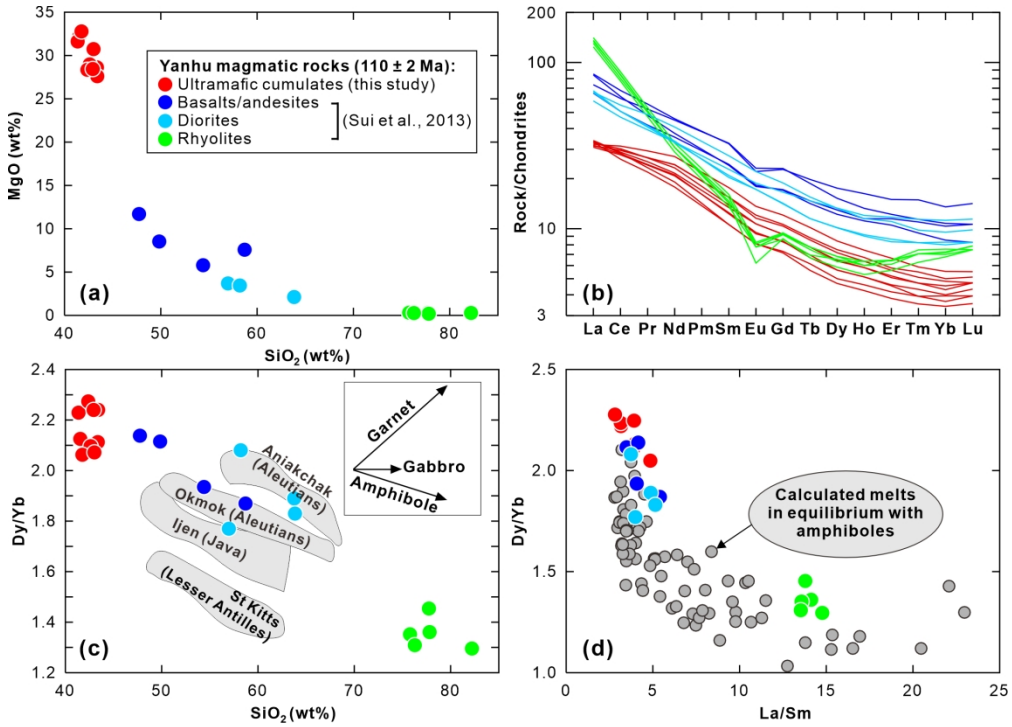

Fig. 6. Major- and trace-element compositions of ultramafic cumulates in this study and basalts, andesites, rhyolites, and diorites reported by Sui et al. (2013). (a) MgO vs. SiO2. (b) Chondrite-normalized REE patterns. Normalizing values are from Sun and McDonough (1989) (c) Dy/Yb vs. SiO2. The data for several active arc volcanoes are from Davidson et al. (2007), which define differentiation trends indicative of amphibole fractionation. The inset shows the effect of fractionation of garnet, amphibole, and gabbro (pyroxene + plagioclase + olivine) on magma compositions (after Davidson et al. (2007)). (d) Dy/Yb vs. La/Sm. Calculated melts in equilibrium with amphiboles in Yanhu cumulates are shown for comparison.

188x135mm (300 x 300 DPI)

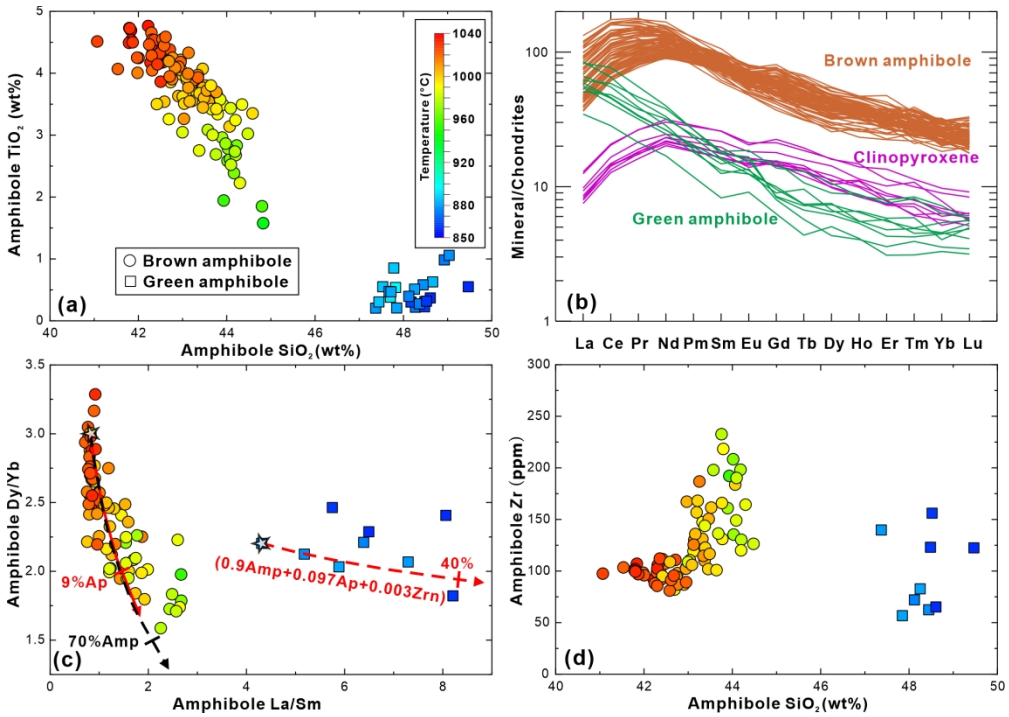

Fig. 7. Major- and trace-element compositions of amphibole in the Yanhu cumulates. (a) TiO2 vs. SiO2. (b) Chondrite-normalized REE patterns. Clinopyroxene inclusions in brown amphibole are plotted for comparison. Normalizing values are from Sun and McDonough (1989). (c) Dy/Yb vs. La/Sm. Arrows with scales indicate the compositional variations of amphiboles resulting from the fractionation of different minerals from their equilibrium melts. Numbers along the arrows denote the amount of fractionating minerals. Mineral abbreviations are the same as in Fig. 2. The black stars represent the starting compositions. (d) Zr vs. SiO2. All data points in (a), (c) and (d) are colour-coded for amphibole crystallisation temperatures obtained from Eq. 5 of Putirka (2016), with the scale displayed in (a).

194x137mm (300 x 300 DPI)

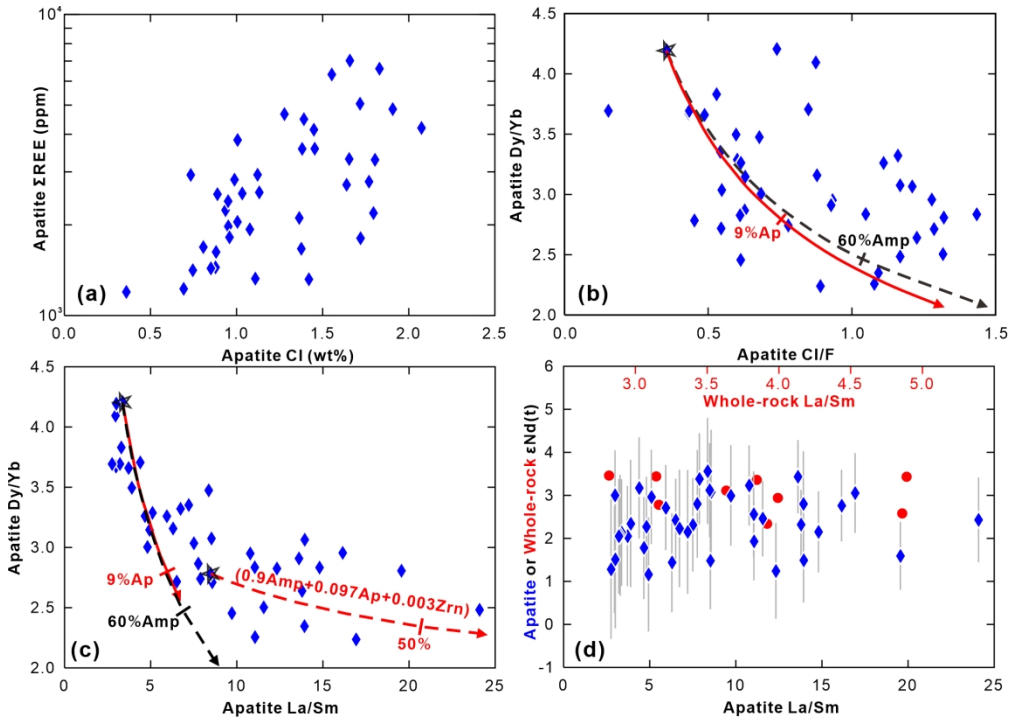

Fig. 8. Major- and trace-element compositions of apatite in the Yanhu cumulates. (a) ΣREE vs. Cl. (b) Dy/Yb vs. Cl/F. (c) Dy/Yb vs. La/Sm. Arrows with scales are the same as those in Fig. 7(c), except that the starting compositions (i.e., black stars) are different. (d) εNd(t) vs. La/Sm. Also shown for comparison are the whole-rock εNd(t) values.

191x136mm (300 x 300 DPI)

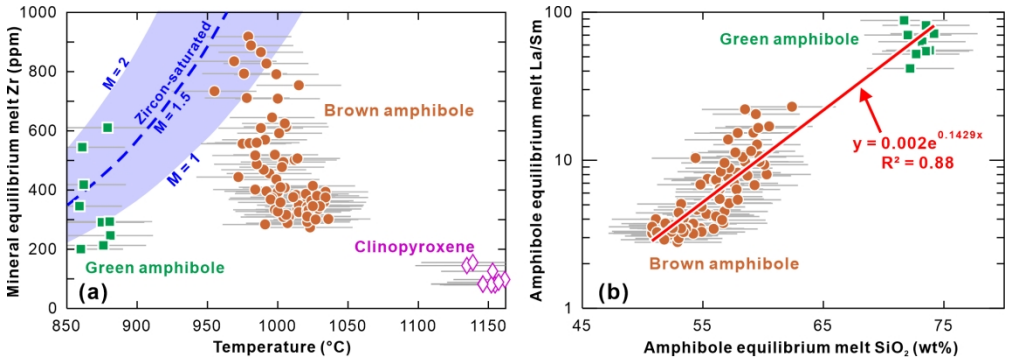

Fig. 9. (a) The crystallisation temperatures of amphibole and clinopyroxene vs. their equilibrium melt Zr contents. Solubility of zircon as function of temperature and melt composition (M = [Na + K + 2Ca]/[Al•Si]) is from Watson and Harrison (1983). (b) La/Sm vs. SiO2 for amphibole equilibrium melts showing the best-fit line. Error bars are 1σ for the calculated temperatures and SiO2 contents.

190x66mm (300 x 300 DPI)

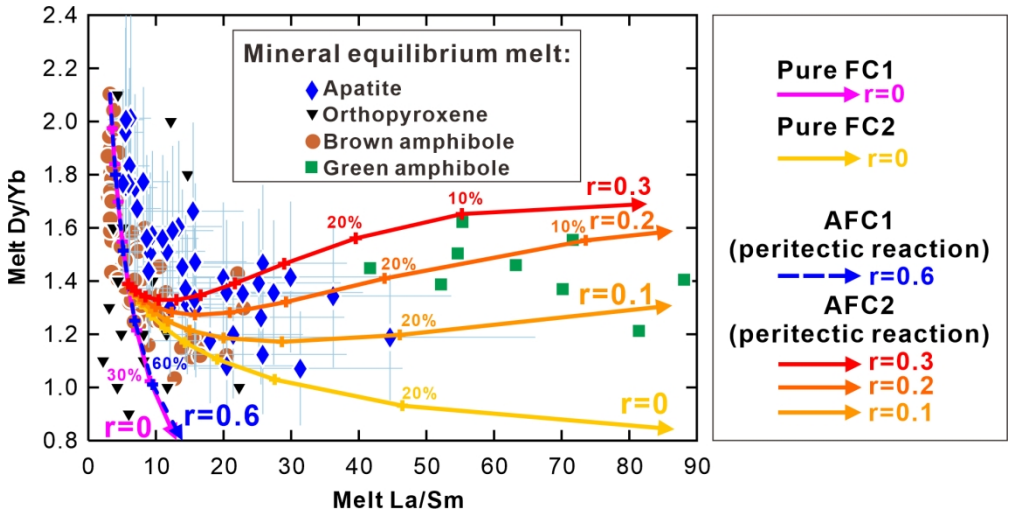

Fig. 10. Geochemical models reproducing the variations in Dy/Yb and La/Sm ratios of the calculated melts in equilibrium with amphibole, orthopyroxene, and apatite. See text for model details and input parameters are given in Table S13. The AFC1 and AFC2 models are performed assuming the following peritectic reactions: Melt1 + 0.89 Ol + 0.11 Cpx = Melt2 + 0.8 Brown Amp + 0.16 Opx + 0.04 Ap (r= 0.6), Melt2 + Brown Amp = Melt3 + 0.9 Green Amp + 0.097 Ap + 0.003 Zrn (r = 0.1, 0.2, 0.3), respectively. The proportions of the assimilated (Ol : Cpx = 8:1) and crystallised (Brown Amp : Opx = 5:1) minerals are assumed based on the modal mineral proportions in thin sections (Table S1). The pure FC1 and FC2 models correspond exactly with the AFC1 and AFC2 models with r = 0, respectively. Errors (2σ) incorporate the uncertainties of DREE values of apatite. Crosses on the modeled curves indicate 10% changes in the fraction of melt remaining.

166x84mm (300 x 300 DPI)

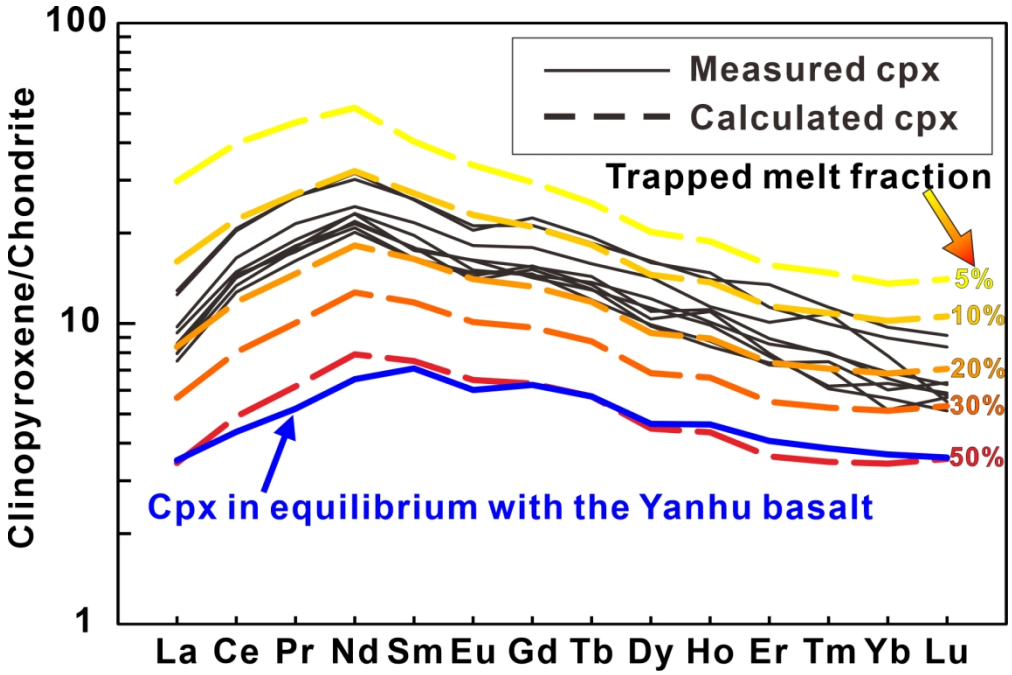

Fig. 11. Chondrite-normalized REE abundances of clinopyroxenes calculated with the method of Bedard (1994) and (2001) assuming the trapped melt fractions (TMF) of 5, 10, 20, 30 and 50%. The proportion of the initial cumulus phases (olivine : clinopyroxene = 8:1) is assumed for all TMF based on the modal mineral proportions in thin sections (Table S1). We used the average abundances of cumulates and crystal/melt partition coefficients from Bedard (2001). The REE pattern of clinopyroxene in equilibrium with a Yanhu high-MgO basalt (YH22-2; Sui et al., 2013) are also reported for comparison.

161x106mm (300 x 300 DPI)

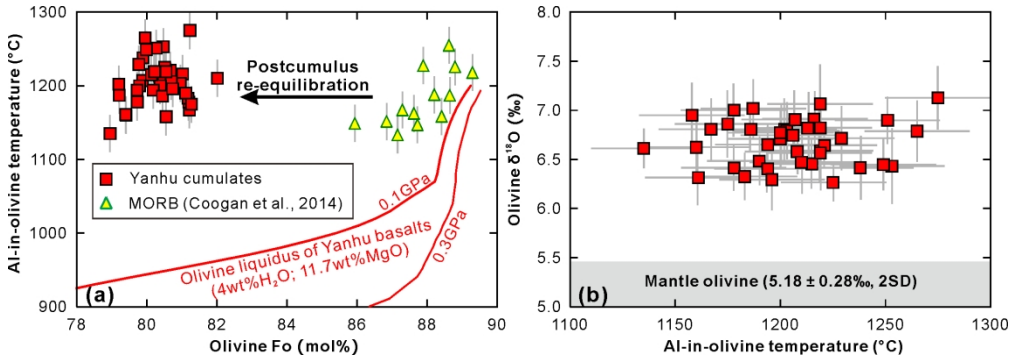

Fig. 12. Al-in-olivine temperature vs. olivine Fo (a) and olivine δ18O values (b). Two red curves show the olivine liquidus of a Yanhu high-MgO basalt (YH22-2; Sui et al., 2013) at 0.1 and 0.3 GPa, which were obtained using Rhyolite-MELTS (Gualda et al., 2012). The Al-in-olivine temperatures of MORB are from Coogan et al. (2014).

199x69mm (300 x 300 DPI)

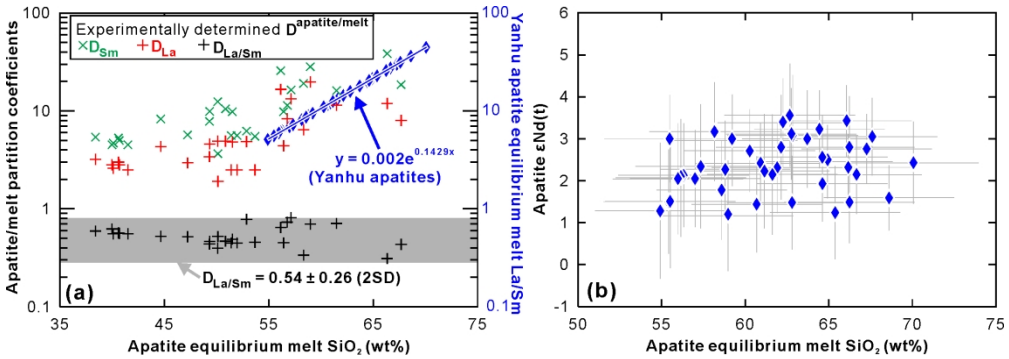

Fig. 13. (a) Apatite/melt DREE and apatite equilibrium melt La/Sm ratios vs. apatite equilibrium melt SiO2 contents. Experimentally determined DREE values are from Prowatke and Klemme (2006) and Watson and Green (1981). (b) Apatite εNd(t) values vs. its equilibrium melt SiO2 contents. Errors (2σ) for calculated SiO2 contents of apatite equilibrium melts incorporate the uncertainties of apatite/melt DLa/Sm (Fig. 13a) and predicted melt SiO2 contents (Fig. 9b) from amphibole chemometry of Putirka (2016).

200x69mm (300 x 300 DPI)

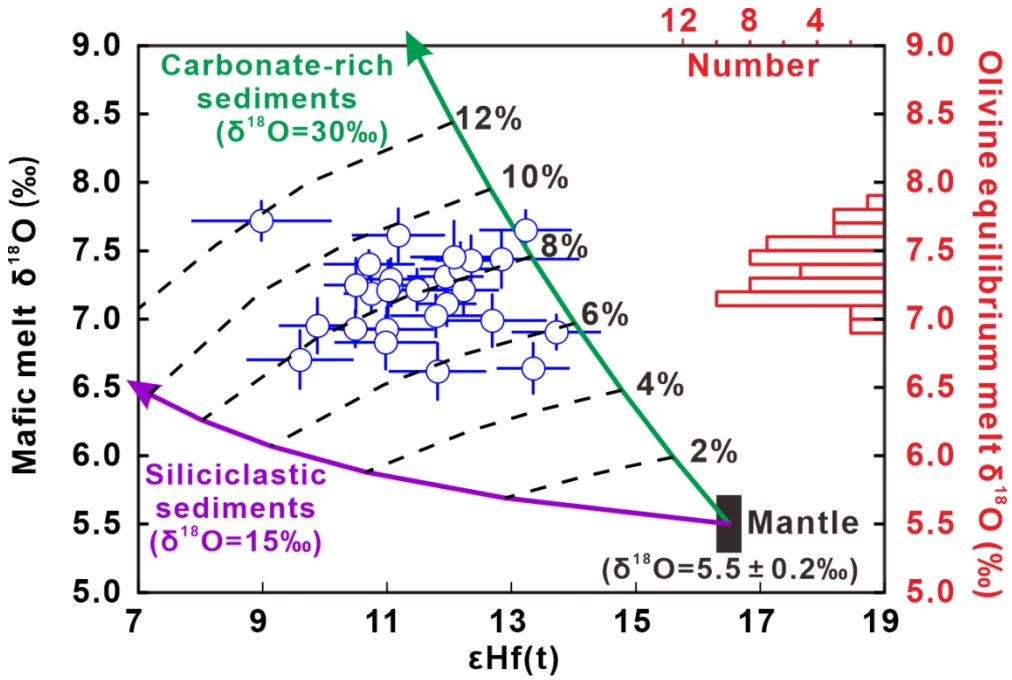

Fig. 14. Calculated δ18O of mafic melts (from the measured δ18O of zircon) vs. εHf(t). Also shown for comparison are the histograms of calculated δ18O values for olivine equilibrium melts. The Δ18O(Melt-Zircon) and Δ18O(Melt-Olivine) fractionation factors were assumed to be 0.5‰ for mafic melts (Valley et al., 2005) and 0.7‰ for mafic melts at 1200°C (Eiler, 2001), respectively. Numbers along the green and purple curves of binary mixing denote the amounts of subducted sediments in the source mantle of Yanhu cumulates. The mantle end-member used in the mixing calculation: εHf(t = 110 Ma) = +16.5 (Griffin et al., 2000), Hf = 0.309 μg/g (Sun and McDonough, 1989), δ18O = 5.5 ± 0.2‰ (Eiler, 2001).

108x72mm (300 x 300 DPI)